Diurnal variations in oxygen and nitrogen isotopes of atmospheric nitrogen dioxide and nitrate: implications for tracing NO_x oxidation pathways and emission sources

Sarah Albertin[1,2], Joël Savarino[2], Slimane Bekki[1], Albane Barbero[2], Roberto Grilli[2], Quentin Fournier[3], Irène Ventrillard[3], Nicolas Caillon[2], Kathy Law[1]

[1]LATMOS/IPSL, Sorbonne Université, UVSQ, CNRS, 75005 Paris, France.
[2]IGE, Univ. Grenoble Alpes, CNRS, IRD, Grenoble INP, 38000 Grenoble, France.
[3]LIPhy, Univ. Grenoble Alpes, CNRS, 38000 Grenoble, France.

Correspondence to: Sarah Albertin (sarah.albertin@univ-grenoble-alpes.fr)

Abstract. The oxygen ($\Delta^{17}O$) and nitrogen ($\delta^{15}N$) isotopic compositions of atmospheric nitrate (NO_3^-) are widely used as tracers of its formation pathways, precursor (nitrogen oxides (NO_x) ≡ nitric oxide (NO) + nitrogen dioxide (NO_2)) emission sources, and physico-chemical processing. However, the lack of observations on the multi-isotopic composition of NO_2 maintains significant uncertainties regarding the quantitative links between the isotopic composition of NO_x and NO_3^-, which ultimately may bias inferences on NO_3^- formation processes and distribution of sources, particularly in winter urban atmospheres. We report here on the first simultaneous atmospheric observations of $\Delta^{17}O$ and $\delta^{15}N$ in NO_2 (n = 16) and NO_3^- (n = 14). The measurements were carried out at sub-daily (~ 3 h) resolution over two non-consecutive days in an Alpine city in February 2021. A strong diurnal signal is observed in both NO_2 and NO_3^- multi-isotopic composition. $\Delta^{17}O$ of NO_2 and NO_3^- ranges from 19.6 ‰ to 40.8 ‰ and from 18.3 ‰ to 28.1 ‰, respectively. During the day and night, the variability of $\Delta^{17}O(NO_2)$ is mainly driven by the oxidation of NO by ozone, with a substantial contribution from peroxy radicals in the morning. NO_3^- mass balance equations, constrained by observed $\Delta^{17}O(NO_2)$, suggest that during the first day of sampling, most of NO_3^- was formed locally from the oxidation of NO_2 by hydroxyl radicals by day, and via heterogeneous hydrolysis of dinitrogen pentoxide at night. For the second day, calculated and observed $\Delta^{17}O(NO_3^-)$ do not match, particularly daytime values; the possible effects on $\Delta^{17}O(NO_3^-)$ of a Saharan dust event that occurred during this sampling period and of winter boundary layer dynamics are discussed. $\delta^{15}N$ of NO_2 and NO_3^- ranges from −10.0 ‰ to 19.7 ‰ and from −4.2 ‰ to 14.9 ‰, respectively. Consistent with theoretical predictions of N isotope fractionation, the observed variability of $\delta^{15}N(NO_2)$ is explained by significant post-emission equilibrium N fractionation. After accounting for this effect, vehicle exhaust is found to be the primary source of NO_x emissions at the sampling site. $\delta^{15}N(NO_3^-)$ is closely linked to $\delta^{15}N(NO_2)$ variability, bringing further support to relatively fast and local NO_x processing. Uncertainties on current N fractionation factors during NO_2 to NO_3^- conversion are underlined. Overall, this detailed investigation highlights the potential and necessity to use

simultaneously $\Delta^{17}O$ and $\delta^{15}N$ in NO_2 and NO_3^- in order to better constrain quantitative inferences on the sources and formation chemistry of NO_3^- in urban environments in winter.

1 Introduction

Despite extensive efforts in emission controls in recent decades, global anthropogenic emissions of nitrogen oxides ($NO_x \equiv$ nitrogen monoxide (NO) + nitrogen dioxide (NO_2)) remain more than two orders of magnitude higher than before the Industrial Revolution (Hoesly et al., 2018). Atmospheric nitrate ($NO_3^- \equiv$ nitric acid (HNO_3) + particulate nitrate (p-NO_3^-)), is the main end-product of NO_x oxidation and a key component of fine particulate matter (PM), which adversely affects human health (WHO, 2021) and contributes to climate change (Masson-Delmotte et al., 2021). NO_3^- can be transported far from emission sources and can be removed from the atmosphere through dry and wet deposition within hours to days (Alexander et al., 2020; Park et al., 2004). The additional input of this "reactive" nitrogen (N_r) into natural environments is known to have detrimental consequences, particularly regarding biodiversity and water quality (Galloway et al., 2008; Vitousek et al., 1997). It is therefore important to have a comprehensive understanding of NO_x emission sources and oxidation processes, on which effective air quality and climate change mitigation strategies rely (e.g., Bauer et al., 2007; Huang et al., 2014; Shah et al., 2018; Tsimpidi et al., 2008; Wang et al., 2013, 2020).

Several studies noted that the response of NO_3^- concentration in air to NO_x emission reduction is contrasted, particularly in winter (e.g., Shah et al., 2018; Tørseth et al., 2012; Wang et al., 2020; Zhou et al., 2019). This is because a variety of factors controls the NO_x conversion efficiency and the NO_3^- content in PM, including precursor emission sources, complex multiphase chemical reactions with other reactive species, and environmental conditions (e.g., temperature, relative humidity, solar radiation) (Zhang et al., 2015). It remain difficult to assess the contribution of each parameter to the non-linear N_r chemistry, which is partly driven by close links between changes in aerosol acidity, gas-particle partitioning, and atmospheric oxidation capacity (Shah et al., 2018; Li et al., 2021b; Fu et al., 2020; Shi et al., 2019). Ozone (O_3) and hydroxyl radicals (OH) (Finlayson-Pitts and Pitts, 2000), are the major oxidants in the atmosphere whose chemical cycles are largely controlled by solar radiation. As a result, there are significant diurnal and seasonal variations in NO_x chemistry (e.g., (Prabhakar et al., 2017; Alexander et al., 2020). Notably, NO_3^- formation is generally dominated by homogeneous OH oxidation and heterogeneous O_3 chemistry during day/summer and night/winter, respectively (Alexander et al., 2020). However, assessing the relative contributions of individual formation channels, together with their sensitivity to environmental parameters, is not straightforward and requires extensive in situ observations combined with modelling tools (e.g., (Alexander et al., 2020; Brown, 2006; Newsome and Evans, 2017; Xue, 2022; Prabhakar et al., 2017).

Upon release into the atmosphere, NO_x, mainly emitted as NO, undergoes oxidation to form NO_2. During the day, a rapid photochemical equilibrium is established between NO and NO_2, known as the "photostationary state" (PSS; Leighton, 1961), via key interconversion reactions (Reactions R1–R3):

$$NO_2 + h\nu \xrightarrow{M} O(^3P) + NO \quad \text{R1}$$

$$O(^3P) + O_2 \xrightarrow{M} O_3 \text{ with } M = N_2 \text{ or } O_2 \quad \text{R2}$$

$$NO + O_3 \rightarrow NO_2 + O_2 \quad \text{R3}$$

This cycle can be disturbed by peroxy radicals ($RO_2 \equiv$ hydroperoxyl radical (HO_2) + methyl peroxy radical (CH_3O_2)) via typically Reaction (R4):

$$NO + RO_2 \rightarrow NO_2 + RO \quad \text{R4}$$

Note that in polluted atmospheres where NO_x mixing ratios often exceed ppb levels, Reaction (R4) followed by Reactions (R1)–(R2) lead to the formation of O_3 (Crutzen, 1979). Although the role of RO_2 in NO_x oxidation is crucial in O_3 formation and NO_x oxidation rate, measuring RO_2 mixing ratio remains challenging due to the need for state-of-the art instrumentation coupled with photochemical models to establish chemical budgets (e.g., (Ren et al., 2006; Tan et al., 2018). While NO is usually oxidised relatively quickly into NO_2 in summer due to the high levels of O_3 and solar radiation, the shorter day length and lower temperature in winter result in a contrasted NO_x cycling. In particular, the formation of a temperature inversion at the surface can trap pollutants emitted close to the surface in a shallow layer for hours to days (e.g., (Largeron and Staquet, 2016; Olofson et al., 2009). Under those conditions, it is not uncommon for O_3 levels to be very low due to quasi-complete titration by NO, which can have further impacts on the atmospheric oxidation capacity. However, pronounced O_3 pollution episodes may also arise in winter in highly polluted areas, such as in oil-producing regions due to intense VOCs emissions (Edwards et al., 2014) or in China, where pollution control strategies mainly target NO_x while VOCs emissions remain more or less constant (Ren et al., 2022). ~~During the daytime~~In urban areas, NO_2 is generally mainly removed from the atmosphere by ~~homogeneous~~ reaction with OH during the day (Dentener and Crutzen, 1993):

$$NO_2 + OH \xrightarrow{M} HNO_3(g) \quad \text{R5}$$

NO_2 can also react with O_3 to form nitrate radicals (NO_3) via Reaction (R6):

$$NO_2 + O_3 \xrightarrow{M} NO_3 + O_2 \quad \text{R6}$$

However, NO_3 is rapidly photolyzed during the day regenerating back NO_2 (Wayne et al., 1991). Another important NO_3 loss reaction~~,~~ is that with NO in polluted environments (Brown and Stutz, 2012). At night, without photolytic activity and

lower precursor emissions, the lifetime of NO_3 radicals substantially increases. NO_3 reacts with NO_2 to form dinitrogen pentoxide (N_2O_5; Reaction R7), which then undergoes heterogeneous hydrolysis to form HNO_3 (Reaction R8):

$$NO_3 + NO_2 \overset{M}{\leftrightarrow} N_2O_5 \quad \text{R7}$$

$$N_2O_5 + H_2O(\text{aerosol}) \rightarrow 2\,HNO_3(aq) \quad \text{R8}$$

Reaction (R7) is temperature dependent, so N_2O_5 can eventually decompose to reform NO_2 and NO_3, with the N_2O_5/NO_3 ratio being negatively correlated with temperature. N_2O_5 is an important nocturnal sink for NO_x, notably in winter in urban atmospheres due to high aerosol loads and low temperatures. However, the efficiency of Reaction (R8) is difficult to determine because it strongly depends on parameters such as the aerosol surface density and its chemical composition (Brown, 2006), which are not often well characterised. In addition, NO_3 can react with hydrocarbons to produce HNO_3, which could significantly contribute to the formation of NO_3^- in industrialised regions with high hydrocarbon emissions (Brown et al., 2011). It is estimated that the Reactions (R1) to (R8) lead to the formation of 82 % of NO_3^- near the surface on a global scale (Alexander et al., 2020). In polluted environments, the respective contributions of Reaction (R5) (OH pathway) and Reactions (R6)–(R8) (N_2O_5 pathway) are more contrasted and are still debated (e.g., Chan et al., 2021; Fu et al., 2020). In addition, the reaction of N_2O_5 with chlorine on aerosols can contribute to NO_3^- production in urban atmospheres (Thornton et al., 2010), with further impacts on O_3 production in continental polluted atmosphere in winter (Wang et al., 2019a). Other reactions, such as those involving halogen and organic intermediates, may become significant for NO_3^- production in specific regions, such as in polar, oceanic, and coastal areas (Alexander et al., 2020; Penkett et al., 2007; Savarino et al., 2013; Simpson et al., 2015).

To help better constrain the atmospheric N_r chemistry and budget, the last three decades have seen a growing interest in stable oxygen (O) and nitrogen (N) isotopes, notably in NO_3^- (Elliott et al., 2019; Savard et al., 2018). The isotopic composition is reported as an isotopic enrichment (δ) with respect to a reference material, defined as $\delta = (R_{sample}/R_{reference} - 1)$, and expressed in per mill (‰). R refers to the elemental abundance ratio of the heavy isotope to the light isotope (e.g., $^{18}O/^{16}O$; $^{17}O/^{16}O$; $^{15}N/^{14}N$) in the sample, and in an international isotopic reference material (Vienna Standard Mean Ocean Water for O; Li et al., 1988, and atmospheric N_2 for N; Mariotti, 1984). A powerful tool to help trace the relative importance of different NO_x to NO_3^- oxidation pathways is through the use of the ^{17}O-excess ($\Delta^{17}O = \delta^{17}O - 0.52 \times \delta^{18}O$). $\Delta^{17}O$ is transferred to NO_3^- by O_3 which possesses a very unique $\Delta^{17}O$ ((26.2 ± 1.3) ‰; Vicars and Savarino, 2014) due to mass-independent fractionation during its formation process (Thiemens, 2006). In comparison, the $\Delta^{17}O$ of other atmospheric oxidants such as OH is near zero due to isotopic exchange with atmospheric water vapor (Dubey et al., 1997). Similarly, as the isotopic anomaly of atmospheric O_2 is very close to 0 ‰ (Barkan and Luz, 2003), and since RO_2 are mostly produced by the reactions R + O_2 and H + O_2, $\Delta^{17}O$ of RO_2 can be considered negligible (Alexander et al., 2020). Therefore,

$\Delta^{17}O$ in NO_3^- represents a unique tracer of the O_3 implication in its formation processes, that can provide valuable constraints on the relative contributions of individual reactions (e.g., Morin et al. 2011, Alexander et al., 2009; Michalski et al., 2003). By a simple mass balance calculation of O atoms in NO_3^-, the ^{17}O-excess of NO_3^- produced by an individual NO_2 to NO_3^- conversion process *i* ($(\Delta^{17}O(NO_3^-)_i)$ can be expressed as:

$$\Delta^{17}O(NO_3^-)_i = \frac{2}{3} \times \Delta^{17}O(NO_2) + \frac{1}{3} \times \Delta^{17}O(\text{add. O})_i \quad (1)$$

where $\Delta^{17}O(NO_2)$ is the ^{17}O-excess of atmospheric NO_2 and $\Delta^{17}O(\text{add. O})_i$ is the transferrable ^{17}O-excess of the oxidant responsible for the conversion of NO_2 in NO_3^- (Michalski et al., 2003). From Eq. (1), if $\Delta^{17}O(NO_2)$ is constrained, one can derive individual $\Delta^{17}O$ transfer to NO_3^- relative to a *i* conversion process and compare this value with observed $\Delta^{17}O(NO_3^-)$.

Recent studies in urban areas have attempted to interpret the variability of $\Delta^{17}O(NO_3^-)$ in aerosols in order to quantify the relative contribution of homogeneous and heterogeneous processes to NO_3^- formation (e.g., Fan et al., 2023, 2022; He et al., 2020, 2018; Li et al., 2022b; Lim et al., 2022; Wang et al., 2023, 2019; Kim et al., 2023; Zhang et al., 2022b). However, to that end, it is necessary to have a clear quantitative understanding of the transfers of $\Delta^{17}O$ in the N_r cycle. To date, due to very limited observational data, there is a lack of well-establish knowledge on the dynamics of $\Delta^{17}O$ in NO_2, the key intermediate species in the formation of NO_3^-. Consequently, strong assumptions about $\Delta^{17}O(NO_2)$ have to be made when interpreting $\Delta^{17}O(NO_3^-)$ measurements, which could potentially lead to biased conclusions. Notably, the most difficult regions for the interpretation of NO_3^- records are potentially polluted areas where the isotopic composition of NO_2 is expected to be highly variable in space and time. Most studies typically estimate $\Delta^{17}O(NO_2)$ during the day by assuming that an isotopic steady state (ISS) is reached between NO_x and O_3 resulting in $\Delta^{17}O(NO_2)$ depending only on the relative contributions of different oxidants to NO oxidation. A recent study reported the first in situ observations of $\Delta^{17}O(NO_2)$ in an urban environment (Grenoble, France) in spring (Albertin et al., 2021). Time resolved NO_2 sampling (ca. 3 h) during 24 h revealed a strong diurnal cycle in $\Delta^{17}O(NO_2)$, reaching ca. 40 ‰ during the day and decreasing down to ca. 20 ‰ at night. The observed $\Delta^{17}O(NO_2)$ values and dial variability were consistent with its expected behaviour derived from $\Delta^{17}O$ mass balance equations under the ISS assumption during the day. However, this first $\Delta^{17}O(NO_2)$ dataset is very short. More measurements are needed to test in different environments and season the applicability of this new isotopic tool and to assess whether the ISS is still valid. At night, the low $\Delta^{17}O(NO_2)$ measured by Albertin et al. (2021) is consistent with the oxidation of freshly emitted NO by O_3. Nonetheless, since the timescale for the oxidation of NO_2 into NO_3^- is thought to exceed the duration of the night (Alexander et al., 2020), it is also common to assume that the isotopic composition of nocturnal NO_2 reflects more daytime formation and conditions of the previous days. While this assumption may hold true in remote areas (Morin et al., 2011), significant uncertainties subsist in urban areas where the nighttime NO_3^- chemistry may be more

efficient. In such circumstances, the production of NO_3^- from NO_2 formed at night would lead to a lower than expected $\Delta^{17}O$ transfer to NO_3^-. For these reasons, the dual survey of the O isotopic composition of NO_2 and NO_3^- would certainly help to accurately interpret $\Delta^{17}O(NO_3^-)$ observations in polluted atmospheres, particularly with sampling at sub-daily time scales which would allow to study the diurnal dynamics of $\Delta^{17}O(NO_2)$ and its links with $\Delta^{17}O(NO_3^-)$.

In addition to $\Delta^{17}O$, $\delta^{15}N$ in NO_3^- ($\delta^{15}N(NO_3^-)$) can be used as a tracer of NO_3^- sources and/or chemical processing. As different NO_x emission sources have often distinct $\delta^{15}N$-fingerprints depending on the NO_x production mechanism (Heaton, 1990; Felix et al., 2012; Fibiger and Hastings, 2016; Walters et al., 2015a, b; Yu and Elliott, 2017; Miller et al., 2018), $\delta^{15}N(NO_3^-)$ is a potentially valuable tool to trace the origins of its gaseous precursor. However, due to N fractionation effects associated with physico-chemical processing, $\delta^{15}N$ is altered during the conversion of NO_x to NO_3^- (Elliott et al., 2019). Therefore, the variability of $\delta^{15}N(NO_3^-)$ can be attributed to: (1) a change in NO_x emission sources and (2) N isotopic fractionations between NO and NO_2, between NO_2 and NO_3^-, and~~/or~~ during the transport of NO_3^-. These effects co-exist with relative contributions varying according to environmental conditions and the mix of NO_x emissions. Numerous observations in diverse environments have emphasised the substantial influence of N fractionation effects in altering the original ^{15}N composition of emitted gaseous NO_3^- precursors (e.g., Bekker et al., 2023; Chang et al., 2018; Geng et al., 2014; Li et al., 2021; Luo et al., 2023; Vicars et al., 2013). Although some N fractionation factors are available from calculations (Walters and Michalski, 2015) and laboratory experiments (Li et al., 2020; Walters et al., 2016), there is still a lack of observational constraints on the magnitude of the N isotopic partitioning between NO_x and NO_3^-, which could lead to biased interpretations of $\delta^{15}N(NO_3^-)$ observations.

Following the preliminary work of Albertin et al. (2021), this study presents for the first time the simultaneous measurements of the atmospheric NO_2 and NO_3^- multi-isotopic compositions. The sampling took place at high temporal resolution (~ 3 h) in late February 2021 in an urban Alpine city. $\Delta^{17}O/\delta^{15}N$ data of NO_2 and NO_3^-, meteorological parameters, and atmospheric observations (NO, NO_2, O_3, and PM) are collated in order to investigate diurnal N_r chemistry, N fractionation effects and NO_x emissions. Our winter measurements extend the atmospheric NO_2 multi-isotopic composition record which is only composed of spring measurements performed during a single day by Albertin et al. (2021). The general aim of this case study is to test NO_2-based isotopic approaches for tracing the origins and fate of NO_x, for instance in urban areas on sub-daily time scales. The added value of $\Delta^{17}O(NO_2)$ measurements in N_r chemistry studies is more critically assessed here than in Albertin et al. (2021) through the use of accurate NO_x measurements. Besides, using the isotopic theoretical framework developed previously, we explore the potential benefits of combining isotopic observations of NO_2 and NO_3^- to gain a more detailed and quantitative on the links between atmospheric N_r chemistry processes and variability in NO_2 and NO_3^- isotopic composition. The framework used in inferring dominant NO_x emission sources from NO_2 $\delta^{15}N$ measurements is also tested.

2 Material and methods

2.1 Study site and sample collection

The study was conducted in February 2021 in Chamonix-Mont-Blanc, France, (45°55′21″ N, 6°52′11″ E; altitude 1035 m above sea level). This narrow (~2 km wide on average in Chamonix) 23 km Alpine valley of about 12,000 inhabitants is surrounded by high-elevation mountains. The city can experience severe PM pollution events during the winter season, mainly due to wood-combustion for domestic heating and road traffic (Chazette et al., 2005; Quimbayo-Duarte et al., 2021; Weber et al., 2018; Aymoz et al., 2007). The study's sampling site was located at a CNRS (Centre National de la Recherche Scientifique) facility in a residential area, 1.2 km south of the Chamonix city centre, and 1.4 km north of the Mont-Blanc tunnel. Ambient air monitoring inlets and off-line gas and aerosol samplers were installed on the facility's terrace, 3 m above the ground level. Over the campaign, the surface was partly covered with snow.

Atmospheric particles (aerosols) were collected using a high-volume sampler (Digitel®, DH77, total suspended particle inlet, 1 m^3 min^{-1}) and glass fiber (GF) filters (Whatman®, 150 mm-diameter). Evaluating the collection efficiency of total NO_3^- has long been debated (e.g., Schaap et al., 2002; Appel et al., 1980) and, although not free from sampling artefacts (e.g., potential volatilisation of HNO_3 after exposure to ambient air), GF filters have been used on several times to study nitrate isotopes, mainly in coastal sites (e.g., Savarino et al., 2007; Michalski et al., 2003; Morin et al., 2009; Frey et al., 2009; Morin et al., 2007a; Patris et al., 2007; Vicars et al., 2013). Under these conditions, the aerosol alkalinity is supposed to allow the collection of HNO_3 (Prospero and Savoie, 1989). In our case, as the ambient air in Chamonix is expected to be free of sea salt, the GF filters were not washed before use in order to keep the initial NaCl coating inherited from the filter manufacturing process. Therefore, in addition to *p*-NO_3^-, we are confident that the high GF filter NaCl loading allowed the quantitative collection of HNO_3 at our site, as it has been shown previously in the literature (Appel et al., 1981); see also our reply and data to the comments of Reviewer #2 on this specific issue). Two field blanks were performed to evaluate the initial content of trace elements and possible contamination during handling. Atmospheric NO_2 was collected concurrently to filter samples using a pre-cleaned honeycomb denuder tube coated with a mixture of 2.5 M KOH (in methanol) and ultrapure guaiacol inserted into a ChemComb® 3500 speciation cartridge (Thermo Scientific®, USA). A second coated denuder was placed in series into the cartridge to check for NO_2 breakthrough. After sampling, denuders were rinsed with 10 mL of deionised water to solubilis~~z~~ed trapped NO_2. Detailed information on the denuder sampling protocol is available in Albertin et al. (2021). Similar to blank filters, two blank denuders were performed. Blank filters and denuders were subjected to same handling, storage, and analytical treatment as field samples. Filters and denuder extractions were stored and transported frozen to IGE (Grenoble, France) for analysis.

Following the objective to investigate the diurnal isotopic composition of NO_2 and NO_3^-, denuder and filter samplings were conducted continuously for 24 hours with sampling time steps ranging from 1:30 to 7:30. During the day, denuder and filter samplings were synchronised. At night, two filter samplings were performed while three sets of denuder tubes were collected. This sampling protocol was conducted during two non-consecutive days, from 19 February 2021 21:00 local time (LT) to 20 February 2021 21:00 LT (sampling period #1 = SP 1) and from 24 February 2021 7:30 LT to 25 February 2021 7:30 LT (sampling period #2 = SP 2).

2.2 Chemical and isotopic analysis

Concentrations of major ions from filter extractions in deionised water were determined by ion chromatography (Thermo Scientific™ Dionex™ Integrion™ HPIC). Reported to the total filter surface, the NO_3^- contribution from blank filters represented on average (8 ± 9) % of sampled NO_3^-. Atmospheric mass concentrations (expressed in μg m^{-3}) were calculated as the ratio of the total ion filter loading (corrected for the blank contribution) to the total volume of air pumped through the filter at STP conditions. NO_2^- concentration in denuder extractions were first estimated using the Griess-Saltzmann reaction and UV–Vis spectrometry at 544 nm. Even though the eluted matrix can interfere with colorimetric analyses, measured concentrations on first denuder tubes were relatively well correlated with ambient NO_2 measurements during atmospheric sampling and allowed to give indications on field blanks and on the volume needed to perform isotopic analysis.

Isotopic analyses were performed using an isotope ratio mass spectrometer (IRMS, Thermo Finnigan™ MAT 253) for analyses of $^{15}N/^{14}N$, $^{17}O/^{16}O$, and $^{18}O/^{16}O$ in NO_3^- and NO_2 samples. Briefly, NO_3^- from filter extractions were converted into gaseous N_2O by the bacterial denitrifier method (Sigman et al., 2001; Casciotti et al., 2002; Kaiser et al., 2007) in which ≈100 nmol of NO_3^- ions were injected into a 2 mL of a bacteria medium (strain of *Pseudomonas aureofaciens*) under anaerobic conditions. NO_2 denuder extractions were treated separately with the azide method (McIlvin and Altabet, 2005; Albertin et al., 2021) in which 2 mL of a sodium azide 2M / acetic acid 100 % buffer were injected into ≈100 nmol of NO_2^- allowing quantitative conversion into N_2O. For both filter and denuder extractions, ions were converted into N_2O which was further thermally decomposed into O_2 and N_2 in a gold tube heated at 850 °C. Then, O_2 and N_2 molecules were separated on a chromatography column and sent separately into the IRMS for the dual analysis of O and N isotopes (see Morin et al., 2009 for more details on the analytical line). The isotopic composition of NO_3^- samples was analysed in triplicate (the mean value of replicate measurements and the associated repeatability are reported in Table S2 in the Supplement). The limited amount of NO_2 samples did not allow for replicate measurements. From UV-vis analysis, all NO_2 samples presented a negligible blank (< 4 %; mean of 1.7 nmol ml^{-1}) except for the sample collected between 13:30 and 16:30 LT during SP 2 which shown a blank around (14.0 ± 1.4) %. Therefore, the measured $\Delta^{17}O$ of this sample was corrected for blank effect assuming that the contaminated NO_2^- possessed a $\Delta^{17}O$ = 0 ‰. No correction from this blank effect was applied on the $\delta^{15}N$

measurements of NO_2 because the $\delta^{15}N$ fingerprint of the contamination could not be characterised. This uncertainty is propagated in the calculations of Section 3 and considered in the discussions. Possible isotopic changes resulting from the conversion and analysis process of NO_3^- and NO_2^- samples were evaluated using international NO_3^- and NO_2^- isotopic reference materials, respectively (Table S3 in the Supplement). Accuracy of the analytical method was estimated as the standard deviation (σ) of the residuals between measurements of the reference materials and their expected values. In our study, average measurement uncertainties on $\delta^{15}N$, $\delta^{17}O$, $\delta^{18}O$, and $\Delta^{17}O$ were estimated to be ±0.3 ‰, ±0.9 ‰, ±1.3 ‰, and ±0.4 ‰, respectively, for NO_3^- samples and ±0.3 ‰, ±0.4 ‰, ±0.9 ‰, and ±0.3 ‰, respectively, for NO_2 samples. Detailed information about the calibration procedure can be found in Morin et al. (2009) and in Albertin et al. (2021) for NO_3^- and NO_2^- samples, respectively.

2.3 Ancillary data

During atmospheric samplings, surface NO_x mixing ratios were measured at the study site using an incoherent broadband cavity-enhanced absorption spectrometer for NO_2 (IBBCEAS; Barbero et al., 2020) and an optical-feedback cavity-enhanced absorption spectrometer for NO (OFCEAS; Richard et al., 2018). PM concentrations (PM_{10} and $PM_{2.5}$) were monitored by an optical particle counter (GRIMM®, EDM 164). O_3 mixing ratio was monitored at the local air quality monitoring site located a kilometre north of the sampling site (Environnement SA®, O3 42M; https://www.atmo-auvergnerhonealpes.fr/, last access: 5 November 2021). Surface temperature ($T_{surface}$) and relative humidity (RH) were measured by a portable logger (Tinytag, TGP-4500, Gemini Data Loggers) located at the air quality monitoring site. Vertical temperatures were measured from 11 similar loggers fixed along the Plan-Praz cable car (45°55′39″ N, 6°51′55″ E) from 1098 to 2021 m above sea level (data obtained from personal communications with C. Coulaud, IGE). The NO_2 photolysis rate (J_{NO_2}) was calculated for the two sampling periods using a photochemical boxmodel (CiTTyCAT version 2.02; Galeazzo et al., 2018; Pugh et al., 2012) using the Fast-J photolysis scheme of Wild et al. (2000) and a surface albedo fixed to 0.65, a value representative of a snow-covered surface (average value between fresh and old snow; more details can be found in Text S1 in the Supplement).

2.4 Interpretation framework for isotopic signals

In this section, we briefly state the key concepts and equations necessary to interpret isotopic signals measured in NO_2 and NO_3^-. A more detailed description and complete equation derivations can be found in cited references.

2.4.1 $\Delta^{17}O$ mass balance equations

Because NO_2 and NO_3^- loss processes do not fractionate in terms of the oxygen mass-independent anomaly and considering that each source reaction induces a transfer of $\Delta^{17}O$ to NO_2 and NO_3^-, one consider the mass conservation of $\Delta^{17}O$ during fractionation processes in the N_r cycle. Hence, one can implement $\Delta^{17}O$ in the general mass balance equation of NO_2 and NO_3^-. An overall expression of the time derivative of $\Delta^{17}O$ in the species X ($\Delta^{17}O(X)$; with X = NO_2 or NO_3^-) is derived as a

function of its deviation from $\Delta^{17}O$ transferred through each production channel i (P_i) ($\Delta^{17}O_i(X)$), weighted according to the relative contributions of the production channels (Vicars et al., 2013):

$$\frac{d}{dt}\left(\Delta^{17}O(X)\right) = \frac{1}{\tau(X)} \times \sum_i \frac{P_i}{\sum_i P_i} \times \left(\Delta^{17}O_i(X) - \Delta^{17}O(X)\right) \quad (2)$$

where P_i expresses reaction rate constant times the atmospheric concentrations of reacting species, and τ is the atmospheric lifetime of the species X at steady state ($\tau = [X]/\sum_i P_i$ with [X] being the atmospheric mixing ratio of the species X).

During the day, the rapid photochemical cycling of NO_x (Reactions R1–R4) leads to an isotopic equilibrium between NO and NO_2, i.e., $\Delta^{17}O(NO) \approx \Delta^{17}O(NO_2)$ (Michalski et al., 2014). Therefore, using the steady state approximation, and considering NO + O_3 (Reaction R3) and NO + RO_2 (Reaction R4) as the main sources of NO_2 at our site, the overall daytime $\Delta^{17}O$ in NO_2 can be expressed by:

$$\Delta^{17}O_{day}(NO_2) \approx T_{NO+O_3} \times \Delta^{17}O_{NO+O_3}(NO_2) \quad (3)$$

where $\Delta^{17}O_{NO+O_3}(NO_2)$ is the O_3 isotopic anomaly transferred to NO through Reaction (R3) (Savarino et al., 2008). T_{NO+O_3}, sometimes named A in the literature, represents the proportion of O atoms originating from O_3 in NO_2, and hence the relative importance of Reaction (R3) in the conversion of NO into NO_2 (Michalski et al., 2003; Morin et al., 2007b; Albertin et al., 2021):

$$T_{NO+O_3} = \frac{k_{NO+O_3}[O_3]}{k_{NO+O_3}[O_3] + k_{NO+RO_2}[RO_2]} \quad (4)$$

where k_{NO+O_3} and k_{NO+RO_2} are the kinetic constants of Reactions (R3) and (R4), respectively. The kinetic constants used in this study are listed in Table A1 in the Appendix. At night, considering that (1) $\Delta^{17}O(NO) \approx 0$ ‰ (NO_x emission without NO_2 recycling), (2) no $\Delta^{17}O$ equilibrium between NO and NO_2 (no photochemical cycling), and (3) O_3 is the main oxidant of NO (no nighttime production of RO_2), $\Delta^{17}O(NO_2)$ is determined by the $\Delta^{17}O$ transfer via Reaction (R3) and by the nighttime residuals of NO_2 formed during the previous daytime hours (Albertin et al., 2021) following:

$$\Delta^{17}O_{night}(NO_2) \approx x \times \Delta^{17}O_{day}(NO_2) + \frac{(1-x)}{2} \times \left(\Delta^{17}O_{NO+O_3}(NO_2) + \Delta^{17}O(NO)\right) \quad (5)$$

where x is the fraction of NO_2 formed during the day to the total NO_2 measured at night.

At our sampling site, we hypothesise Reaction (R5) (OH pathway) and Reactions (R6)–(R8) (N_2O_5 pathway) as the main daytime and nighttime NO_3^- production channels, respectively. At steady state, from Eq. (2), we derive general expressions for $\Delta^{17}O$ in NO_3^- during the day and night, associated with the OH and N_2O_5 pathways, respectively (Alexander et al., 2020):

$$\Delta^{17}O_{day}(NO_3^-) \approx \frac{2}{3} \times \Delta^{17}O_{day}(NO_2) \quad (6)$$

$$\Delta^{17}O_{night}(NO_3^-) \approx \frac{2}{3} \times \Delta^{17}O_{night}(NO_2) + \frac{1}{6} \times \Delta^{17}O_{NO_2+O_3}(NO_3) \quad (7)$$

where $\Delta^{17}O_{NO_2+O_3}(NO_3)$ is the ^{17}O-excess transfer from O_3 to NO_3 during Reaction (R6) (Berhanu et al., 2012). Without wet scavenging, dry deposition is the main sink of NO_3^- (Park et al., 2004). Assuming a mean NO_3^- deposition velocity of 0.5 cm s^{-1} (mean value of the dry deposition velocities of HNO_3 and *p*-NO_3^-; Zhang et al., 2009), and considering the maximum daytime and minimum nighttime boundary layer heights of 500 and 100 m above ground level, respectively (estimations based on measured vertical temperature profiles; Fig. S2 in the Supplement), the estimated residence time of NO_3^- against dry deposition can reach up to 28 hours during the day, and 6 hours at night (Table B1). Therefore, on ~~a~~ sub-daily time scales, the ^{17}O-excess in NO_3^- during the day is more likely to reflect a combination of daytime and nighttime production processes than during the night. Note that, our estimated residence times for NO_3^- against dry deposition are upper limits as they represent the time required to reduce by a factor e the concentration of NO_3^- present at the top of the boundary layer; NO_3^- close to the surface would have a much shorter residence time.

2.4.2 Nitrogen isotopic fractionation effects

Each source of NO_x generates a $\delta^{15}N$ fingerprint which depends on the type and conditions (temperature and pressure) of combustion, and on the type of fuel (e.g., coal, oil, gas) (Heaton, 1990; Felix et al., 2012; Fibiger and Hastings, 2016; Walters et al., 2015a, b; Yu and Elliott, 2017; Miller et al., 2018). The mean $\delta^{15}N$ of NO_x ($\delta^{15}N(NO_x)$) emitted in the atmosphere results from the sum of each NO_x emission $\delta^{15}N$ fingerprint weighted by their relative contribution to the total NO_x emissions. Once in the atmosphere, NO_x is subjected to oxidation processes and isotopic exchanges that alter the initial $\delta^{15}N(NO_x)$. As a result, $\delta^{15}N$ in NO_2 and in NO_3^- is a complex function of both the $\delta^{15}N$ signature of NO_x emissions and N isotopic effects. These latter can be categorised into three groups: (1) the equilibrium isotope effect (EIE), (2) the kinetic isotope effect (KIE), and (3) the photochemical isotope fractionation effect (PHIFE) (Miller and Yung, 2000; Young et al., 2002). The magnitude of these isotopic effects is quantified as ^{15}N enrichment factor (ε), which is defined as ($\alpha - 1$), where α represents the N isotopic fractionation factor.

A general expression for $\delta^{15}N(NO_2)$ can be derived as a function of a factor F_N which represents the overall N isotopic fractionation effects between NO_x emissions and NO_2 (expressed in ‰), the fraction of NO_2 with respect to NO_x (f_{NO_2} = $[NO_2]/[NO_x]$), and of $\delta^{15}N(NO_x)$ (Albertin et al., 2021; Li et al., 2020):

$$\delta^{15}N(NO_2) = F_N \times (1 - f_{NO_2}) + \delta^{15}N(NO_x) \quad (8)$$

Therefore, the ^{15}N isotopic shift between $\delta^{15}N(NO_2)$ and $\delta^{15}N(NO_x)$ is given by:

$$\delta^{15}N(NO_2) - \delta^{15}N(NO_x) = \Delta^{15}(NO_2 - NO_x) = F_N \times (1 - f_{NO_2}) \quad (9)$$

Physico-chemical processes between NO and NO_2 can preferentially promote or deplete ^{15}N in NO_2 with respect to emissions of NO_x (i.e., $\delta^{15}N(NO_2) \neq \delta^{15}N(NO_x)$). The importance of this fractionation shift is modulated by the factor $(1 - f_{NO_2})$. When NO is almost entirely converted into NO_2 ($f_{NO_2} \approx 1$), N fractionation effects can be neglected (i.e., $\delta^{15}N(NO_2) \approx \delta^{15}N(NO_x)$).

From samples collected at Jülich, Germany, Freyer et al. (1993), observed for the first time the linear relation described by Eq. (8), and set the theoretical framework to interpret $\delta^{15}N$ variabilities in atmospheric NO_2. They showed that the observed seasonal variation of $\delta^{15}N(NO_2)$ was driven by N fractionation effects (represented in the F_N factor) caused by photochemistry and isotopic equilibrium. Based on this work, and that of Li et al. (2020), Albertin et al. (2021) derived an expression of F_N during the day assuming that the NO-NO_2 system is in isotopic equilibrium (steady-state):

$$(F_N)_{day} \approx \frac{\alpha_{LCIE}{}^{*} A^{*}{}_{day} + (\alpha_{EIE(NO_2/NO)} - 1)}{A^{*}{}_{day} + 1} \quad (10)$$

with $\alpha_{LCIE}{}^{*} = \alpha_{KIE(NO+O_3)} - \alpha_{PHIFE}$

and $A^{*}{}_{day} = \frac{J_{NO_2}}{k_{NO+NO_2}[NO]}$

where $\alpha_{LCIE}{}^{*}$ is the fractionation factor of combined KIE and PHIFE (LCIE is for Leighton Cycle Isotope Effect), and $\alpha_{EIE(NO_2/NO)}$ is the EIE fractionation factor between NO and NO_2. $\alpha_{EIE(NO_2/NO)}$ and $\alpha_{KIE(NO+O_3)}$ are temperature dependent and can be calculated following the theoretical approach of Walters and Michalski (2015) (Table D1). From calculations based on the zero point energy of $^{15}NO_2$ and the absorption cross section of $^{14}NO_2$, α_{PHIFE} is estimated to vary between 1.0020 and 1.0042 for a range of solar zenith angles between 90 ° and 0 ° (Fang et al. 2021). In this study we use a mean value of α_{PHIFE} at 1.0031. $A^{*}{}_{day}$ is defined as the ratio of the NO_2 lifetime with respect to isotopic exchanges over the

daytime NO_2 chemistry lifetime. J_{NO_2} is the NO_2 photolysis rate, k_{NO+O_3} is the rate constant of Reaction (R3), and k_{NO+NO_2} is the rate constant of the isotopic exchange $^{15}NO_2 + {}^{14}NO \rightarrow {}^{14}NO_2 + {}^{15}NO$. During the day, $\Delta^{15}(NO_2 - NO_x)$ varies according to the environmental conditions. In low-NO_x conditions (e.g., remote and polar regions) $\Delta^{15}(NO_2 - NO_x)$ is predicted to be controlled by LCIE factors ($A^*_{day} >> 1$), whereas an EIE-dominated regime ($A^*_{day} << 1$) is expected in polluted environments (high-NO_x conditions). At night, J_{NO_2} and α_{PHIFE} are null and A^*_{night} is defined as the ratio of NO lifetime with respect to isotopic exchange with NO_2 to NO chemical lifetime at night $\left(A^*_{night} = \frac{k_{NO+O_3}[O_3]}{k_{NO+NO_2}[NO_2]}\right)$. In this study, we consider only one particular case with $A^*_{night} << 1$, which means that isotopic exchanges are much faster than NO oxidation by O_3. In this scenario, KIE effects are negligible compared to EIE effects and $(F_N)_{night}$ can be expressed as:

$$(F_N)_{night} \approx \frac{(\alpha_{EIE(NO_2/NO)} - 1)}{\alpha_{EIE(NO_2/NO)}} \quad (11)$$

The complete derivation of Eqs. (10) and ~~Eq.~~ (11) is given in Albertin et al. 2021.

KIE and EIE are also expected during the conversion of NO_2 to NO_3^-. The ^{15}N partitioning associated to isotopic equilibrium between N_2O_5 and NO_2 (Reaction R7) can be theoretically computed as a function of temperature (Walters and Michalski, 2015; Table D1). At 298 K, if N isotopic equilibrium is reached, N_2O_5 is predicted to have $\delta^{15}N$ values 27.6 ‰ higher than NO_2. Considering that the NO_2/NO_3^- isotopic fractionation through the N_2O_5 pathway is solely controlled by EIE, NO_3^- is therefore expected to be enriched in ^{15}N relative to NO_2. However, to date, no experimental study has reported on ^{15}N partitioning between atmospheric NO_2 and NO_3^-, and the fractionation factors are still being debated (Freyer 1991, Fang et al. 2021). The dominant NO_x to NO_3^- conversion processes considered in this study, along with corresponding $\Delta^{17}O$ transfer factors and the known ^{15}N enrichment factors at 298 K (determined from both experimental and computational studies) are illustrated in Figure C1.

3 Results and Discussion

3.1 Temporal variations of general atmospheric observations

Surface temperatures during SP 1 and SP 2 show similar values, with a marked diurnal cycle (from −2 °C to 16 °C; Figure 1). A positive temperature gradient with altitude is observed from late evening to morning. Surface temperature rises around midday and reaches a maximum at around 15:00 LT, resulting in a negative temperature gradient with altitude. In deep Alpine valleys, the diurnal variability of surface air temperature is strongly influenced by the temporal evolution of the boundary layer structure, particularly in winter with the formation of a surface layer inversion (Whiteman, 1982). As previously observed in Chamonix (Chazette et al., 2005), the nocturnal surface layer inversion regularly thickens during the

night of the sampling periods. After sunrise, air masses warm up until the nocturnal inversion layer breaks down in the late morning. Observed RH behaviour relatively correlates with the increase in temperature during the day, showing a rapid decrease between mid-morning and early afternoon (from 96 % to 23 % and from 96 % to 30 % for SP 1 and SP 2, respectively; Figure 1).

During SP 1 and SP 2, the mixing ratios of NO, NO_2 and O_3 exhibit diurnal patterns (Figure 1) typical in Chamonix in late February (Figure S3 in the Supplement), and more generally in urban areas (Mayer, 1999). The highest NO level is observed in the morning, peaking around 10:30 LT (82 nmol mol^{-1} and 152 nmol mol^{-1} for SP 1 and SP 2, respectively). The concurrent increase in NO_2 and decrease in O_3 (down to 1 nmol mol^{-1}) can be attributed to Reaction (R3) ($NO + O_3$). NO_x decreases in the late morning, likely due to a combination of lower emissions, NO_2 oxidation, and dilution effect. Meanwhile, O_3 gradually recovers to ca. 30 nmol mol^{-1}, a typical winter background air level in Europe (Gaudel et al., 2018). Due to local emissions, NO_x increases again from 16:00 LT, resulting in O_3 titration, and subsequently to an increase in NO_2 (up to 40 nmol mol^{-1}). After 18:30 LT, NO remains low until the morning, and NO_2 decreases slowly until midnight, stalls around 10 nmol mol^{-1}, and then rises again at 5:30 LT. After the late afternoon titration, O_3 gently recovers and stay relatively low throughout the night likely due to a titration effect from nocturnal NO emissions which are confined in the surface layer inversion.

Both SP 1 and SP 2 show diurnal variations in PM mass concentrations (Figure 1), with morning and evening peaks related to local emissions from traffic and home heating (Aymoz et al., 2007). PM_{10} concentrations display an additional increase at midday following the breakdown of the temperature inversion. At 12:30 LT, while PM_{10} concentrations increase moderately during SP 1 to reached 38.6 µg m^{-3}, a sharp increase to 119 µg m^{-3} is observed during SP 2. Then PM_{10} concentrations decrease during the afternoon of SP 1, but remain high during the afternoon of SP 2 until the surface inversion layer forms. On average, PM_{10} concentration is three times higher during SP 2 ((59.4 ± 37.6) µg m^{-3}) than during SP 1 ((20.6 ± 10.2) µg m^{-3}). The considerable increase in PM_{10} concentrations between SP 1 and SP 2 is likely to be explained by a Saharan dust episode that started on February 23 (Fig. S3, S4, and S5 in the Supplement). Saharan dust deposition is a well-known phenomenon in the Alps, which is characterised by a sudden increase of coarse particles, mainly composed of alumino-silicates as well as calcium and potassium (Angelisi and Gaudichet, 1991; Delmas, 1994; Di Mauro et al., 2019; Goudie and Middleton, 2001; Greilinger et al., 2018; Schwikowski et al., 1995; Sodemann et al., 2006).

The NO_3^- mass concentration varies from 0.3 µg m^{-3} to 3.4 µg m^{-3}, with an average of (0.9 ± 0.6) µg m^{-3} for SP 1 and of (1.2 ± 0.9) µg m^{-3} for SP 2 (Figure 1). During both sampling periods, NO_3^- concentration is within the range of previous observations made in Chamonix in winter (Allard, 2018). NO_3^- shows a distinctive peak at 3.4 µg m^{-3} during SP 2 between 10:30 and 13:30 LT, correlated with the PM_{10} surge. During transport, dust can undergo heterogeneous uptake and

conversion of gases on its surface, leading to the inclusion of secondary species such as NO_3^-, sulfate, and ammonium (Usher et al., 2003). NO_3^- on dust results mainly from HNO_3 uptake and heterogeneous reactions of N_2O_5 (see Usher et al., 2003 for a review and references therein). Mineral dust is believed to significantly contribute to NO_3^- formation and size distribution, particularly in regions close to dust emission sources (Karydis et al., 2016). However, the origin of NO_3^- during SP 2 at our site remains unclear and could be attributed to the advection of both nitrated-dust particles formed through heterogeneous processes during transport and anthropogenic fine particles (Aymoz et al. 2004).

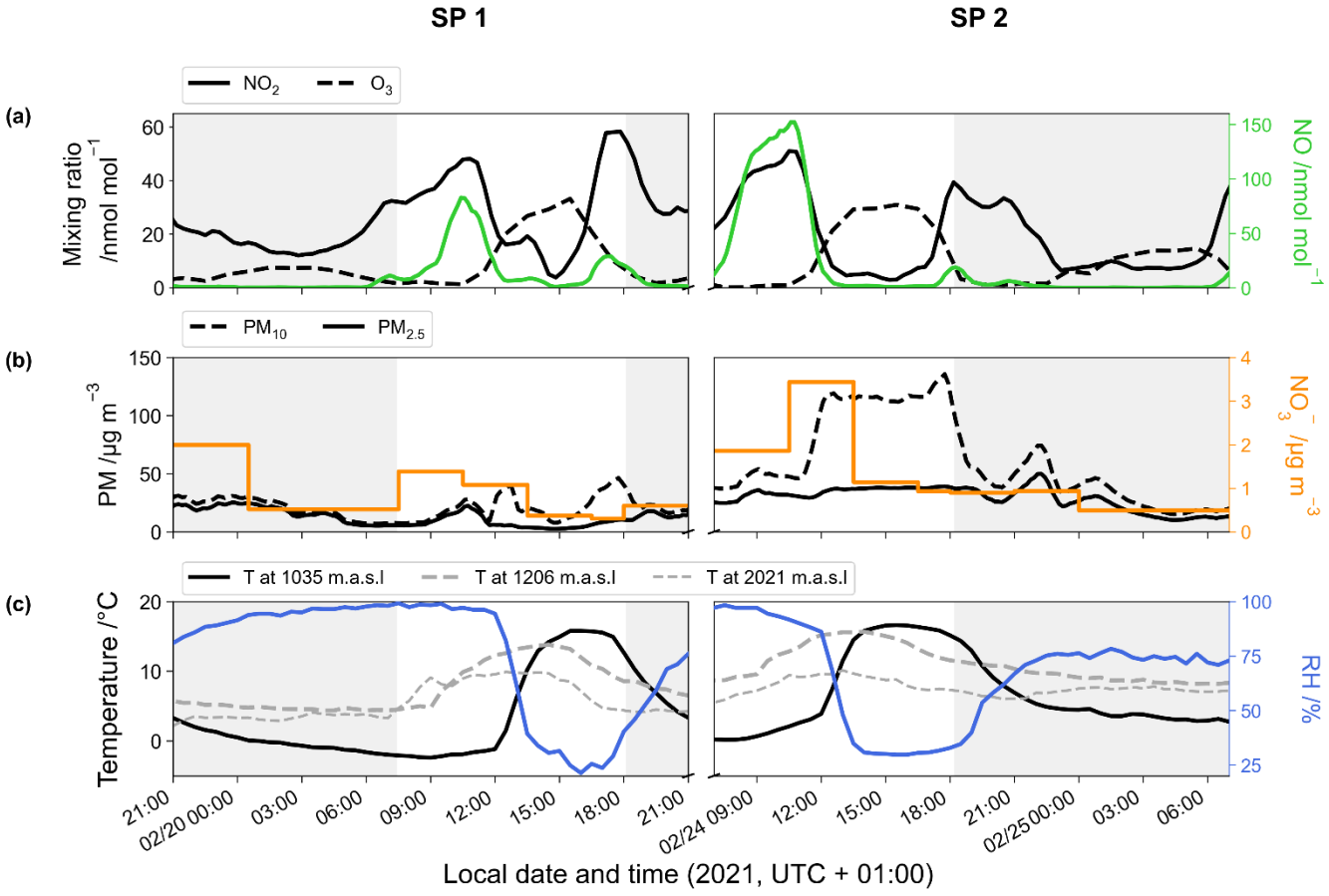

Figure 1. Temporal evolution of the 1-hour rolling mean of **(a)** NO_2 (black line), O_3 (dashed line), and NO (green line) mixing ratios, **(b)** PM (dashed line for PM_{10} and solid line for $PM_{2.5}$) and NO_3^- (orange horizontal line) mass concentrations, and **(c)** temperature at the surface (black line), at 1206 m (dashed grey line), and at 2021 m (light dashed grey line) and surface relative humidity (blue line). Data were collected during the two sampling periods (SP 1 and SP 2) in Chamonix. Grey backdrop shaded areas represent the nighttime (sunset to sunrise).

Figure 2 shows the temporal evolution of measured $\Delta^{17}O$ and $\delta^{15}N$ of NO_2 and NO_3^- in Chamonix during the two sampling periods (SP 1 and SP 2). All isotopic data used in this study are reported in Table S1 and Table S2 in the

Supplement. In the following analysis, first we describe $\Delta^{17}O(NO_2)$ measurements and gives interpretation in light of NO_x chemistry cycling (Section 3.2). Then, an analysis of $\Delta^{17}O(NO_3^-)$ measurements is proposed aggregating daytime and nighttime periods and comparing them with $\Delta^{17}O(NO_3^-)$ estimates derived from $\Delta^{17}O(NO_2)$ measurements and $\Delta^{17}O$ mass balance for major chemical processes (Section 3.3). In light of these results and atmospheric conditions during SP 1 and SP 2, sub-daily $\Delta^{17}O(NO_3^-)$ dynamics are investigated. In Section 3.4, N fractionation effects in the NO_x cycle are quantified, and the dominant NO_x emission source is identified. The dynamics of $\delta^{15}N(NO_3^-)$ is also described and its use to trace NO_x emission sources and oxidation processes is discussed.

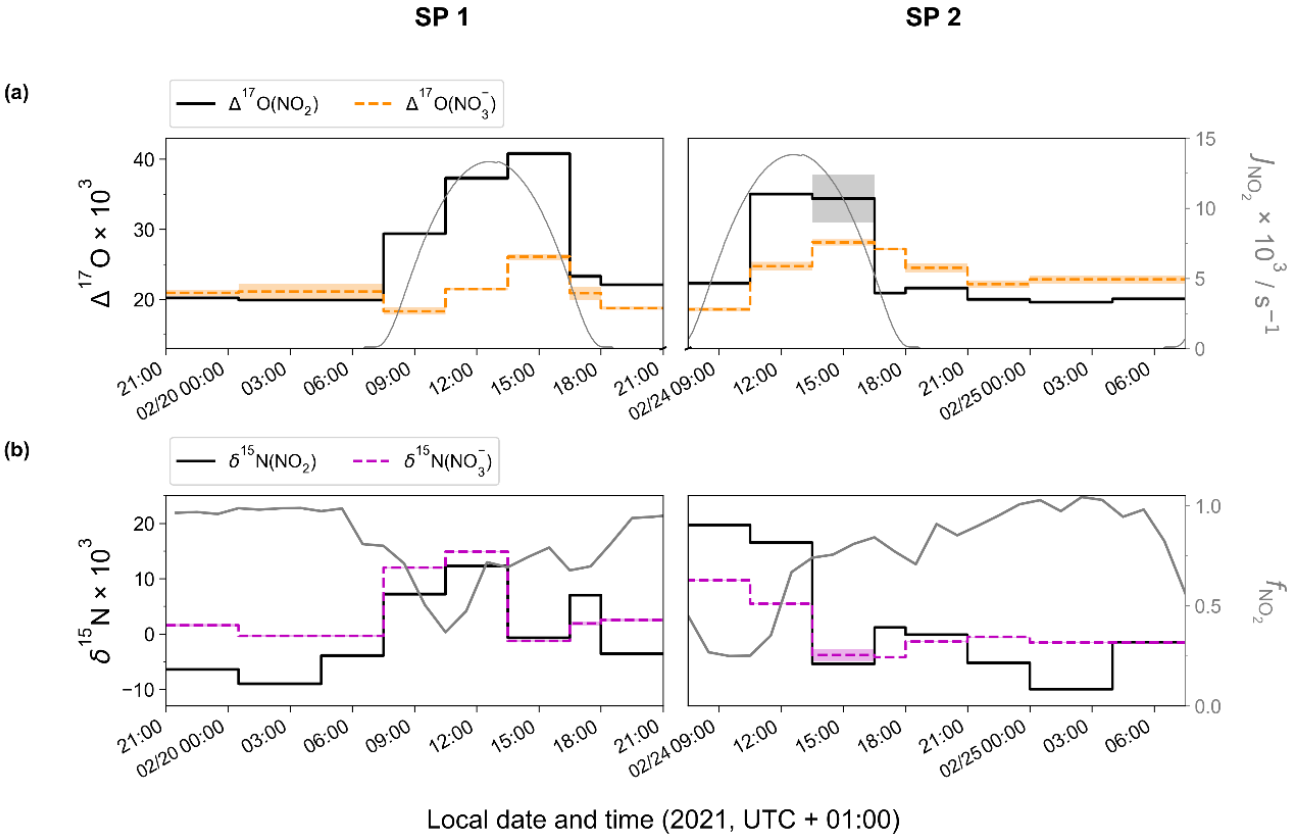

Figure 2. Temporal evolution of observed **(a)** $\Delta^{17}O$ and **(b)** $\delta^{15}N$ of atmospheric NO_2 (top and bottom solid black horizontal line) and NO_3^- (top orange and bottom magenta horizontal dashed line) in Chamonix (length of horizontal line = sampling period, shaded area = overall analytical error). The NO_2 photolysis rate ($\boldsymbol{J_{NO_2}}$, top grey line) is from CiTTyCAT boxmodel output. $\boldsymbol{f_{NO_2}}$ ($\boldsymbol{f_{NO_2}}$ = [NO_2] / ([NO_2] + [NO]); bottom grey line) is calculated from hourly mean mixing ratio of NO and NO_2.

3.2 $\Delta^{17}O$ of NO_2 and NO_x diurnal cycling

Over the course of SP 1 and SP 2, $\Delta^{17}O(NO_2)$ shows a large diurnal variability (from 19.6 ‰ to 40.8 ‰) with a weighted mean ± one standard deviation of (25.2 ± 7.1) ‰. $\Delta^{17}O(NO_2)$ values during the day (7:30–18:00 LT, (28.5 ± 7.3) ‰) are

significantly higher (p-value = 0.002, n = 16) than during the night (18:00–7:30 LT, (20.8 ± 1.0) ‰). By day, $\Delta^{17}O(NO_2)$ follows a similar increasing trend during SP 1 and SP 2, reaching a respective maximum of 40.8 ‰ between 13:30–16:30 LT and 35.0 ‰ between 10h30–13h30 LT. For both sampling periods, after sunset, $\Delta^{17}O(NO_2)$ stabilises between 21:00 and 7:30 LT at ca. 20 ‰. Using the same sampling methodology in a mid-latitude urban area in spring, Albertin et al. (2021) reported very similar $\Delta^{17}O(NO_2)$ values over the course of one day (20.5–39.2 ‰), following a comparable diurnal pattern. As presented above (Section 2.4.1), according to the ISS (isotopic steady state) framework, the variability of $\Delta^{17}O(NO_2)$ reflects changes in the relative contributions of Reaction (R3) (NO + O_3) and Reaction (R4) (NO + RO_2) to the overall production of NO_2. At our site, $\Delta^{17}O(NO_2)$ drops rapidly during the 16:30–18:00 LT interval to 23.3 ‰ and 20.9 ‰ during SP 1 and SP 2, respectively. Since, the isotope recycling rate in the NO_x-O_3 system is driven at first order by J_{NO_2} (Michalski et al., 2014), due to low solar radiation between 16:30–18:00 LT at our site, such a rapid drop of $\Delta^{17}O(NO_2)$ suggests that sampled NO_2 might not be at ISS anymore when the NO_2 photolysis is very slow, notably at the end of the day in winter. Therefore, we only consider that ISS holds between 7:30 and 16:30 LT in order to avoid the questionable end-of-the day measurements in our ISS-based analysis. At night (i.e., no ISS), the observed drop of $\Delta^{17}O(NO_2)$ in the early evening reflects the rapid replacement of NO_2 formed during the day by NO_2 produced during the night via the conversion of freshly emitted NO, in line with Eq. (5). Then, high NO_2 throughout the night, along with relatively low O_3, supports observations of low $\Delta^{17}O(NO_2)$ at night (i.e., ≈20 ‰).

Using Eq. (3), we derive from $\Delta^{17}O(NO_2)$ observations the relative contribution of Reaction (R3) (NO + O_3) to Reaction (R4) (NO + RO_2) in the formation of NO_2 (T_{NO+O_3}):

$$T_{NO+O_3} = \frac{\Delta^{17}O_{day}(NO_2)}{\Delta^{17}O_{NO+O_3}(NO_2)} \quad (12)$$

Between 7:30 and 16:30 LT, T_{NO+O_3} varies from 0.55 to 1.00 (**Erreur ! Source du renvoi introuvable.**), with a mean of 0.88 and 0.75 for SP 1 and SP 2, respectively. The NO + O_3 pathway is dominant between 13:30 and 16:30 LT, corresponding to the time when O_3 is highest (Figure 1). In contrast, the maximum contribution for the NO + RO_2 pathway is observed between 7:30 and 10:30 LT, when NO levels are high and rising continuously. Interestingly, previous studies reported a high sensitivity of RO_2 to changes in NO_x, particularly at high NO_x levels (Ren et al., 2006; Stone et al., 2012). Sources of RO_2 in wintertime are mainly driven by the production of OH radicals from HONO photolysis, alkene ozonolysis, and formaldehyde photolysis (Tan et al., 2018). During winter, HONO plays a crucial role in NO_x/O_3/RO_2 chemistry, particularly in the morning, as its photolysis can potentially accelerate daytime oxidation processes, leading to increased RO_2 production (Alicke et al., 2003; Aumont et al., 2003). Direct emissions from vehicle exhaust could be significant a source of VOCs and HONO at our site (Brulfert et al., 2005; Gu et al., 2019; Kirchstetter et al., 1996; Kurtenbach et al., 2001; Liu et

al., 2023). Heterogeneous processes on ground surfaces and aerosols can also contribute to HONO formation (Aumont et al., 2003). In addition, snowpack releases may also be a potential source of HONO (Grannas et al., 2007), as detected in Paris after a snow event, which could significantly impact the urban OH budget (Michoud et al. 2015).

Following the approach of Albertin et al. (2021), combining Eqs. (3) and (4) allows to derive RO_2 mixing ratio from observed $\Delta^{17}O(NO_2)$ and O_3 mixing ratio following:

$$[RO_2] = \frac{k_{NO+O_3}[O_3]}{k_{NO+RO_2}}\left(\frac{\Delta^{17}O_{NO+O_3}(NO_2)}{\Delta^{17}O_{day}(NO_2)} - 1\right) \quad (13)$$

Between 7:30 and 16:30 LT, we estimate an average RO_2 mixing ratio at our site of (0.88 ± 0.88) pmol mol^{-1} and (4.92 ± 5.16) pmol mol^{-1} during SP 1 and SP 2, respectively (**Erreur ! Source du renvoi introuvable.**). Studies conducted in urban winter environments reported RO_2 measurements at a few pmol mol^{-1} (Ren et al., 2006; Emmerson et al., 2005; Tan et al., 2018; Kanaya et al., 2007), in good agreement with our estimations. Similarly, RO_2 mixing ratios derived by Albertin et al. (2021) from observed $\Delta^{17}O(NO_2)$ in spring (mean of (13.8 ± 11.2) pmol mol^{-1}) were also found to be in line with studies conducted in the same season. The fact that our isotopic inference of RO_2 mixing ratios carried out in two different seasons (winter and spring) are both comparable to direct in situ RO_2 measurements confirm the sensitivity of our method in probing the $NO_x/O_3/RO_2$ chemical dynamics. We think that our method may be very valuable in deciphering oxidation processes of N_r species, down to sub-daily temporal scales. Nonetheless, we recognise that without concurrent in situ measurements of RO_2 and $\Delta^{17}O(NO_2)$, it is not possible to validate unambiguously the quantitative estimation of RO_2 levels with our method.

Sampling interval (start - end)	T_{NO+O_3}	RO_2 /pmol mol^{-1}
SP 1		
20/02 07:30 - 20/02 10:30	0.72 ± 0.01	0.86 ± 0.75
20/02 10:30 - 20/02 13:30	0.91 ± 0.01	1.77 ± 0.36
20/02 13:30 - 20/02 16:30	1.00 ± 0.01	0.00 ± 0.91
Mean	*0.88*	*0.88*
Std dev.	*0.14*	*0.88*
SP 2		
24/02 07:30 - 24/02 10:30	0.55 ± 0.01	0.58 ± 1.67
24/02 10:30 - 24/02 13:30	0.86 ± 0.01	3.56 ± 0.50
24/02 13:30 - 24/02 16:30	0.84 ± 0.08	10.63 ± 6.75
Mean	*0.75*	*4.92*
Std dev.	*0.18*	*5.16*

Table 1. T_{NO+O_3} and RO_2 mixing ratio (mean value ± overall uncertainty) derived from the isotopic measurements.

At this point, it is important to recall that the choice of the $\Delta^{17}O_{NO+O_3}(NO_2)$ in Eq. (12) is of a particular importance for quantifying T_{NO+O_3} (as for RO_2) In the literature, $\Delta^{17}O_{NO+O_3}(NO_2)$ varies between 35 ‰ and 41 ‰ (Michalski et al., 2003; Savarino et al., 2016; Vicars et al., 2012; Li et al., 2022a; Zhang et al., 2022b). This relatively wide range of values is partly a result of some confusion in defining $\Delta^{17}O_{NO+O_3}(NO_2)$, the $\Delta^{17}O$ transfer from O_3 to NO. Indeed, the term $\Delta^{17}O(O_3^*)$ is sometimes erroneously used as the transfer function of $\Delta^{17}O$ from O_3 to NO_2 during Reaction (R3). $\Delta^{17}O(O_3^*)$ is actually defined as $\Delta^{17}O$ of O_3 terminal atoms and is also named $\Delta^{17}O(O_3)_{term}$ in the literature. As the $\Delta^{17}O$ in O_3 is borne by its terminal atoms, $\Delta^{17}O(O_3^*) = 1.5 \times \Delta^{17}O(O_3)_{bulk}$. However, $\Delta^{17}O_{NO+O_3}(NO_2)$ can be equal to $1.5 \times \Delta^{17}O(O_3)_{bulk}$ if only terminal atoms of O_3 reacts with NO. But laboratory experiments by Savarino et al. (2008) did show that O_3 does react with NO not solely with its terminal atoms but also, to a small but significant extent, with its central atom (probability of (8 ± 5) % for the abstraction of central atoms during the reaction NO + O_3). Consequently, $\Delta^{17}O_{NO+O_3}(NO_2)$ is slightly lower than $1.5 \times \Delta^{17}O(O_3)_{bulk}$ and the $\Delta^{17}O_{NO+O_3}(NO_2)$ expression determined by Savarino et al. (2008) should be used: $\Delta^{17}O_{NO+O_3}(NO_2) = 1.18 \pm 0.07 \times \Delta^{17}O(O_3)_{bulk} + (6.6 \pm 1.5)$ ‰.

Assuming that their maximum measured daytime $\Delta^{17}O(NO_2)$ reflects the conversion of NO to NO_2 only through Reaction (R3) (i.e., $T_{NO+O_3} = 1$), Albertin et al. (2021) derived a $\Delta^{17}O_{NO+O_3}(NO_2)$ value of 39.2 ‰ from Eq. (3). Given the respective analytical uncertainties (around ±1 ‰), their value is in very good agreement with the maximum daytime value of 40.8 ‰ we observed in Chamonix. Similarly to Albertin et al. (2021), assuming that the highest daytime $\Delta^{17}O(NO_2)$ value at our site corresponds to $T_{NO+O_3} \approx 1$ leads to $\Delta^{17}O_{NO+O_3}(NO_2) = 40.8$ ‰. Using the experimental $\Delta^{17}O_{NO+O_3}(NO_2)$ transfer function determined by Savarino et al. (2008), we estimate a bulk ^{17}O-excess of O_3 ($\Delta^{17}O(O_3)_{bulk}$) at (29.0 ± 2.2) ‰. This value is consistent with the range of direct $\Delta^{17}O(O_3)_{bulk}$ measurements at mid-latitudes (mean of (26.2 ± 1.3) ‰; Vicars and Savarino, 2014), although falling at the upper end of the range. Interestingly, Vicars and Savarino (2014) reported a significant peak in $\Delta^{17}O(O_3)_{bulk}$ during February-March in Grenoble, France (located 120 km southwest of Chamonix), based on year-round measurements with $\Delta^{17}O(O_3)_{bulk}$ values 2–3 ‰ higher than the annual mean of 26.2 ‰. Although the cause of increased values during this period is unknown, our derived $\Delta^{17}O(O_3)_{bulk}$ matches remarkably well the February-March measurements reported by Vicars and Savarino (2014).

3.3 Interpretation of $\Delta^{17}O$ in atmospheric nitrate

Over the two sampling periods, $\Delta^{17}O(NO_3^-)$ varies significantly (from 18.3 ‰ to 28.1 ‰), with a weighted mean of (22.5 ± 3.1) ‰. While $\Delta^{17}O(NO_2)$ values are relatively similar during the two sampling periods, $\Delta^{17}O(NO_3^-)$ values are systematically higher during SP 2 than during SP 1, except during the 7:30–10:00 LT interval. $\Delta^{17}O(NO_3^-)$ in Chamonix is in the same range of most previous observations in urban environments (9–44 ‰; e.g., Kim et al., 2023; Wang et al., 2023;

Fan et al., 2023; Zhang et al., 2022b; Lim et al., 2022; Li et al., 2022b), but lower than most values measured during the cold season which are typically >25 ‰. Unlike $\Delta^{17}O(NO_2)$, daytime and nighttime $\Delta^{17}O(NO_3^-)$ values at our site are not significantly different (p-value > 0.05, n = 14). Similarly, from 12 h resolved sampling in winter Beijing, He et al. (2018) found no significant difference between daytime and nocturnal $\Delta^{17}O(NO_3^-)$ and suggest that each sample reflects NO_3^- produced during both the day and night. From high-time-resolved (3 h) aerosol sampling in winter Beijing, Zhang et al. (2022b) reported $\Delta^{17}O(NO_3^-)$ values between 23.4 ‰ to 39.3 ‰, with higher values observed at night ((31.0 ± 2.6) ‰) than during the day ((29.3 ± 3.0) ‰). This ~~diel~~ diurnal behaviour of $\Delta^{17}O(NO_3^-)$ was attributed to the changes in the branching ratio of nocturnal and photochemical reactions on NO_3^- formation. In Chamonix, the range of $\Delta^{17}O(NO_3^-)$ values are very different from Zhang et al. (2022b) observations, with consistently lower values and a distinct diurnal tendency. However, in the cases of $\Delta^{17}O(NO_3^-)$ measurements at sub-daily temporal scale, the atmospheric lifetime of NO_x and NO_3^- is critical for comparing $\Delta^{17}O(NO_3^-)$ records from one site to another. Pollutant levels and atmospheric conditions between Chamonix and Beijing are very different, notably in winter when Asian urban areas can experience severe haze pollution episodes with NO_3^- mass concentration exceeding 70 μg m^{-3}, which is over 10 times higher than in Chamonix (Lim et al., 2022; He et al., 2018; Zhang et al., 2022b). In such conditions, PM can reach several hundreds of μg m^{-3} for several days, which can significantly impact atmospheric processes involved in the formation of secondary species. Aside from the intrusion of Saharan dust during SP 2, the pollutant level in Chamonix is indicative of a moderately polluted region, with significant diurnal variations.

3.3.1 Steady state evaluation of $\Delta^{17}(NO_3^-)$

To investigate the factors influencing the variability of $\Delta^{17}O(NO_3^-)$ at our site, one compare observed $\Delta^{17}O(NO_3^-)$ with estimated values of $\Delta^{17}O(NO_3^-)$ derived from $\Delta^{17}O$ mass balance and observed $\Delta^{17}O(NO_2)$, assuming the OH and N_2O_5 pathways dominate the formation of NO_3^- at our site. Therefore, calculated $\Delta^{17}O(NO_3^-)$ reflect the theoretical $\Delta^{17}O$ transfer during the oxidation of NO_2 to NO_3^- at our site through the dominant chemical process during the day (i.e. OH pathway) and at night (i.e. N_2O_5 pathway).

As presented, during the day, we consider that the conversion of NO_2 into NO_3^- is predominantly influenced by Reaction (R5) (OH pathway). Hence, the theoretical corresponding ^{17}O-excess transfer to NO_3^- is estimated using Eq. (6) and observed $\Delta^{17}O(NO_2)$ between 7:30 and 18:00 LT (n = 3 per sampling period). Then, in order to estimate a daytime average value of $\Delta^{17}O(NO_3^-)$ which is representative of the potential for the formation of NO_3^- from surface NO_2 by the OH pathway, each calculated $\Delta^{17}O(NO_3^-)$ is weighted by the product $[NO_2]\times J_{NO_2}$ (the diurnal variability of the OH mixing ratio is assumed to follow the diurnal J_{NO_2} variation; Liu et al., 2021). Finally, an overall mean daytime $\Delta^{17}O(NO_3^-)$ for SP 1 and SP 2 is estimated by taking the sum of the weighted calculated values ($=\Delta^{17}O_{calc}(NO_3^-)$). The same approach is used during

the night, assuming that the conversion of NO_2 into NO_3^- is dominated by Reactions (R6)–(R8) (N_2O_5 pathway). Eq. (7) and observed $\Delta^{17}O(NO_2)$ between 18:00 and 7:30 LT (n = 3 per sampling day) are used to estimate $\Delta^{17}O(NO_3^-)$. Each calculated $\Delta^{17}O(NO_3^-)$ is weighted by the product $[NO_2]\times[O_3]$ (i.e., NO_3 production rate) and summed to estimate a mean nighttime $\Delta^{17}O(NO_3^-)$ for SP 1 and SP 2. The ^{17}O-excess transferred from O_3 to NO_2 during Reaction (R6) ($\Delta^{17}O_{NO_2+O_3}(NO_3)$) is fixed at 44.7 ‰. This value is set accordingly to the transfer function reported by Berhanu et al. (2012) whereby $\Delta^{17}O_{NO_2+O_3}(NO_3) = (1.23 \pm 0.19) \times \Delta^{17}O(O_3)_{bulk} + (9.02 \pm 0.99)$ and $\Delta^{17}O(O_3)_{bulk} = 29.0$ ‰ (see Section 2.4.1). We compare hereafter $\Delta^{17}O_{calc}(NO_3^-)$ with the weighted day and night averages of observed $\Delta^{17}O(NO_3^-)$ at our site. During the day, $\Delta^{17}O_{calc}(NO_3^-)$ is compared with $\Delta^{17}O(NO_3^-)$ observations averaged between 7:30 and 18:30 LT (n = 3). At night, $\Delta^{17}O_{calc}(NO_3^-)$ is compared with $\Delta^{17}O(NO_3^-)$ observations averaged between 18:30 to 7:30 LT.

At night during SP 1, observed $\Delta^{17}O(NO_3^-)$ and $\Delta^{17}O_{calc}(NO_3^-)$ are in good agreement ($\Delta^{17}O_{calc}(NO_3^-) - \Delta^{17}O(NO_3^-) = \Delta^{17}(NO_{3\,calc}^- - NO_{3\,obs}^-) = 0.9$ ‰), suggesting a local and rapid (< 12 h) conversion of NO_2 into NO_3^- via the N_2O_5 pathway. During the day, observed $\Delta^{17}O(NO_3^-)$ is 0.5 ‰ higher than $\Delta^{17}O_{calc}(NO_3^-)$, also suggesting that NO_3^- is formed locally during the day for oxidation of surface NO_2 through the OH pathway. Small differences between observed and calculated $\Delta^{17}O$ of NO_3^- during the day/night could be explained by the presence of NO_3^- residues formed during the previous night/day, which are not considered in the calculations since they do not account for NO_3^- lifetime. In contrast to SP 1, $\Delta^{17}O_{calc}(NO_3^-)$ during SP 2 is significantly lower than the mean observed $\Delta^{17}O(NO_3^-)$, particularly during the day with a $\Delta^{17}(NO_{3\,calc}^- - NO_{3\,obs}^-)$ of –6.4 ‰. The significant gap between observed and calculated $\Delta^{17}O(NO_3^-)$ suggests a different origin and/or formation process of NO_3^- during SP 2 compared to SP 1. Although less important than during the day, $\Delta^{17}O_{calc}(NO_3^-)$ values for SP 2 at night is lower by 2.2 ‰ to the observed value. This small shift can be explained by residuals of enriched daytime NO_3^-. It is important to point out that, although the NO_2 sample collected on Feb 24 between 13:30 and 16:30 LT presents an important blank (ca. 14 %), ambient NO_2 is low during the sampling period (mean of (4.5 ± 1.8) nmol mol^{-1}). Therefore, as each $\Delta^{17}O$ value used to estimate $\Delta^{17}O_{calc}(NO_3^-)$ is weighted by the mean ambient NO_2 mixing ratio over the sampling period, the incertitude related to this blank has little influence on the daily average of $\Delta^{17}O_{calc}(NO_3^-)$. Given the low $\Delta^{17}(NO_{3\,calc}^- - NO_{3\,obs}^-)$ during SP 1, observed $\Delta^{17}O(NO_3^-)$ can be explained by the local and rapid (< 12 h) oxidation of NO_2, dominated by the OH and N_2O_5 pathway during the day and night, respectively. However, in contrast to SP 1, the ^{17}O-excess measured in NO_3^- during the day of SP 2 cannot be fully constrained by the oxidation of surface NO_2 through the OH pathway, suggesting that the formation mechanisms of NO_3^- are different between SP 1 and SP 2 and/or the presence of NO_3^- not formed locally during SP 2. Below we examine the changes in the sub-daily dynamics of $\Delta^{17}O(NO_3^-)$ between SP 1 and SP 2 in light of atmospheric observations.

		$\Delta^{17}O(NO_2)$ /‰	$\Delta^{17}O_{calc}(NO_3^-)$ /‰	$\Delta^{17}O(NO_3^-)$ /‰	$\Delta^{17}(NO_3^-{}_{calc} - NO_3^-{}_{obs})$
Daytime (7:30-18:00)	SP 1	30.0 ± 7.3	22.5 ± 4.6	23.0 ± 3.1	–0.5
	SP 2	26.1 ± 6.9	17.5 ± 4.6	23.9 ± 3.8	–6.4
Nighttime (18:00-7:30)	SP 1	21.2 ± 1.1	21.4 ± 0.7	20.5 ± 1.1	0.9
	SP 2	20.8 ± 1.0	21.0 ± 0.6	23.2 ± 1.0	–2.2

Table 2. Mean observed $\Delta^{17}O$ data of NO_2 ($\Delta^{17}O(NO_2)$) and NO_3^- ($\Delta^{17}O(NO_3^-)$) in Chamonix, and mean calculated $\Delta^{17}O$ of NO_3^- ($\Delta^{17}O_{calc}(NO_3^-)$) using Eqs. (6) and (7) at day and night, respectively, constrained with observed $\Delta^{17}O(NO_2)$. Day and night calculated values were weighted by $[NO_2]\times J_{NO_2}$ and $[NO_2]\times[O_3]$, respectively

3.3.2 $\Delta^{17}(NO_3^-)$ sub-daily dynamics

Between 7:30–10:30 LT, $\Delta^{17}O(NO_3^-)$ is very similar during SP 1 (18.3 ‰) and SP 2 (18.6 ‰). Nonetheless, on the following sampling time step (i.e., between 10:30–13:30 LT), $\Delta^{17}O(NO_3^-)$ is significantly different between SP 1 (21.5 ‰) and SP 2 (24.7 ‰). Intriguingly, between 7:30–13:30 LT, $\Delta^{17}O(NO_2)$ during SP 2 (26.9 ‰) is lower compared to SP 1 (32.8 ‰). As a consequence, if one consider that NO_3^- is formed from the oxidation of local NO_2 through identical pathways during SP 1 and SP 2, observed $\Delta^{17}O(NO_3^-)$ should be lower during SP 2 than during SP 1. Therefore, the more pronounced increase of observed $\Delta^{17}O(NO_3^-)$ during the 10:30–12:30 LT interval of SP 2 suggests a different origin and/or formation channel of NO_3^-, as mentioned previously. One more piece of evidence is that, during this period of time, PM_{10} and NO_3^- levels increase significantly during SP 2, alongside the disruption of the inversion layer (depicted in Figure 1). It can be inferred that this rise in PM_{10} is mostly due to the presence of Saharan dust. The simultaneous increase of NO_3^- and of $\Delta^{17}O(NO_3^-)$ corroborates the hypothesis that this NO_3^- was not formed from the oxidation of ambient NO_2. Furthermore, such an increase in $\Delta^{17}O(NO_3^-)$ can only be supported by the oxidation of NO_2 through the N_2O_5 pathway, which is not expected to be important during the day due to the rapid photolysis of NO_3 and its titration by NO (Brown and Stutz, 2012).

Interestingly, aerosol samplings conducted at various heights (8 m, 120 m, and 260 m above ground level) in Beijing, China, revealed a positive vertical gradient of $\Delta^{17}O(NO_3^-)$ in winter, from on average 29 ‰ to 33 ‰ (Fan et al., 2022). In summer, the $\Delta^{17}O(NO_3^-)$ values at the three altitudes were very similar. This increase of $\Delta^{17}O(NO_3^-)$ with altitude in winter was believed to result from a stratification of NO_2 to NO_3^- oxidation processes due to low vertical mixing and elevated surface NO_x emissions. However, the authors did not consider the potential variability of $\Delta^{17}O(NO_2)$ with altitude, which can be substantial in urban areas at night as low $\Delta^{17}O(NO_2)$ results from surface NO oxidation. For our study, we propose an alternative interpretation of the vertical variability of $\Delta^{17}O(NO_3^-)$, where $\Delta^{17}O(NO_2)$ is considered as the main driver. During the formation of the nocturnal boundary layer, NO_2 formed during the day can be trapped above the surface layer in the

nocturnal residual layer (NRL). This NO_2 has a high $\Delta^{17}O$ because it was formed during the previous daytime hours under the ISS framework (Eq. (3)). Throughout the night, this highly enriched NO_2 (ca. 37 ‰ which is the average of the maximum $\Delta^{17}O(NO_2)$ during SP 1 and SP 2) can be converted to NO_3^- via the N_2O_5 pathway, hence leading to a substantial $\Delta^{17}O$ transfer to NO_3^- at around 32 ‰, which is in the range of $\Delta^{17}O(NO_3^-)$ observed by Fan et al. (2022) in winter. In the meantime, NO emitted at the surface during the night can be converted to NO_2 by O_3, with a $\Delta^{17}O$ transfer of ca. 20 ‰ (Eq. (5) with $x = 0$). This low enriched NO_2 can be further oxidised to NO_3^- by the N_2O_5 pathway which results in a $\Delta^{17}O$ transfer at around 21 ‰. This NO_2 with a low $\Delta^{17}O$ is very likely to be formed only at the surface during the night in areas experiencing important NO_x emissions (Michalski et al., 2014). Furthermore, surface NO_2 with low $\Delta^{17}O$ is not expected to be transported aloft as it is formed in the surface inversion layer during the night. Therefore, NO_3^- formed in the NRL during winter nights may be more enriched than the NO_3^- formed concurrently at the surface, regardless of the NO_2 oxidation process involved. When the inversion layer breaks during the following day, the NO_3^- that was formed in the NRL during the night is mixed with the NO_3^- formed at the surface, resulting in an increase in the overall surface $\Delta^{17}O$. In this scenario, the presence of the Saharan dust during SP 2 may have increased the NO_3^- loading aloft by promoting heterogeneous processes on aerosol surfaces in the vicinity of Chamonix. Hence, NO_2 stratification at night could explain the observed increase in $\Delta^{17}O$ of NO_3^- at the surface following the collapse of the nocturnal inversion layer. However, we cannot determine whether the enriched NO_3^- were formed in the vicinity of Chamonix and/or transported to our site by Saharan dust.

Although the exact nature of the high ^{17}O-excess measured in NO_3^- during SP 2 remains unclear, boundary layer dynamics is thought to play a significant role in the variability of $\Delta^{17}O(NO_3^-)$ at the surface due to the stratification of NO_2. Therefore, a wider consideration of such factors should be explored to avoid possible over-interpretation of $\Delta^{17}O(NO_3^-)$ variabilities at the surface, especially in urban areas experiencing significant boundary layer dynamics in winter and high surface emissions of NO_x at night. Measuring $\Delta^{17}O(NO_2)$ at various altitudes could provide better insights on the vertical dynamics of $\Delta^{17}O(NO_3^-)$, and subsequently quantitative information on NO_3^- production processes.

3.4 Nitrogen isotopic compositions

3.4.1 N fractionation effects in the NO_x cycle

Over the two sampling periods, $\delta^{15}N(NO_2)$ shows substantial diurnal variability (from −10.0 ‰ to 19.7 ‰, n = 16) with a weighted mean of (4.0 ± 9.1) ‰. In contrast, Albertin et al. (2021) reported a weak diurnal fluctuation of $\delta^{15}N(NO_2)$ in spring in Grenoble, in a narrow range from about −12 ‰ to −10 ‰. In summer in an urban/suburban location, Walters et al. (2018) also observed a wide range of $\delta^{15}N(NO_2)$ values, however, unlike our study, these are almost consistently negative

(from −31.4 ‰ to 0.4 ‰) with an overall mean at (−11.4 ± 6.9) ‰. As shown in Eq. (8), fluctuations in $\delta^{15}N(NO_2)$ reflect changes in NO_x emission sources and/or N fractionation effects, these latter being weighted by $1 - f_{NO_2}$ i.e., the more NO_x is under the form of NO, the greater the N fractionation effects (see Section 2.4). Hence, in the previous works of Albertin et al. (2021) and Walters et al. (2018), due to high f_{NO_2} (> 0.7), isotope effects were small (<2.7 ‰) and $\delta^{15}N(NO_2)$ was mostly driven by changing contribution of NO_x emission sources. At our site, f_{NO_2} shows a wider range, from 0.3 to 1.0, suggesting significant N isotopic fractionation effects, with minimum and maximum contributions corresponding to the highest and lowest observed value of $\delta^{15}N(NO_2)$, respectively. This pronounced seasonal behaviour of N isotope fractionation effects within the NO_x cycle has previously been outlined in the seminal study of Freyer et al. (1993). Overall, compared with summer, lower f_{NO_2} during winter months due to lower O_3 concentrations and higher NO_x emissions favour EIE between NO and NO_2, which also has a higher fractionation factor due to the lower temperatures (see Appendix D: Equilibrium N fractionation factors). Besides, this seasonal fluctuation of f_{NO_2} can be expected to be observed on smaller time scales, typically on the diurnal scale in urban areas where NO is generally fully oxidised into NO_2 at night due to a lower NO_x emission rate resulting in higher f_{NO_2} at night than during the day, as observed at our sampling (Figure 2).

Figure 3 shows the linear dependence of $\delta^{15}N(NO_2)$ on $(1 - f_{NO_2})$ over the two sampling periods, indicating the significant influence of atmospheric processes that alter the N isotopic distribution during the conversion of NO_x into NO_2. The linear regression gives a slope and an intercept of about (43.6 ± 3.3) ‰ and (−8.8 ± 1.0) ‰, respectively. According to Eqs. (10) and (11), the linearity between daytime (07:30−18:00 LT) and nighttime (18:00−07:30 LT) values suggests that EIE dominates the N fractionation processes between NO_x and NO_2. The influence of LCIE during the day could explain the greater variability around the linear fit in the daytime observations.

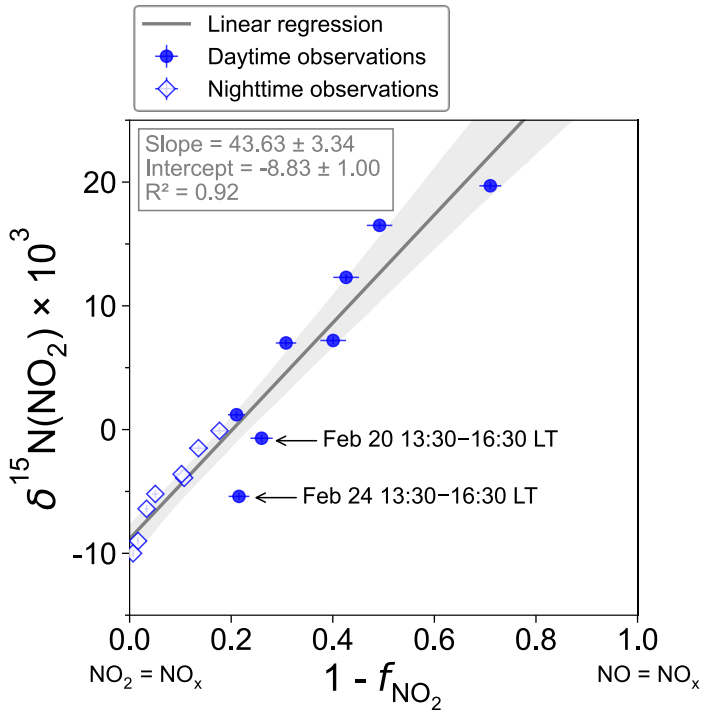

Figure 3. Correlation plot of δ^{15}N of atmospheric NO_2 vs. $(1 - f_{NO_2})$ from observations in Chamonix in February 2021. f_{NO_2} are averaged over the collection period of each NO_2 sample. The grey shade is the 95 % confidence interval. White diamonds and blue dots represent the nighttime (18:00−07:30 LT) and daytime (07:30−18:00 LT) observations, respectively. The linear regression is plotted over the nighttime and daytime observations.

The relative importance of EIE and LCIE in the N fractionation between emitted NO_x and NO_2 is assessed by calculating the A^* factor during the day (7:30–18:00 LT; A^*_{day}) and night (18:00–7:30 LT; A^*_{night}) (

Sampling interval (start – end)	$A^{*(1)}$	$F_N^{(2)}$	f_{NO_2}	$\Delta^{15}(NO_2 - NO_x)^{(3)}$ /‰	$\delta^{15}N(NO_x)$ /‰
GP #1					
20/02 13:30 – 20/02 16:30	0.46 ± 0.08	25.00 ± 2.27	0.74 ± 0.02	6.5 ± 0.9	−7.2 ± 0.9
24/02 13:30 – 24/02 16:30	2.09 ± 0.39	6.90 ± 1.97	0.78 ± 0.02	1.5 ± 0.4	−6.9 ± 0.6
Mean	*1.27*	*16.39*	*0.76*	*4.1*	*−7.1*
Std dev	*1.14*	*12.58*	*0.03*	*3.5*	*0.2*
GP #2					
19/02 21:00 – 20/02 00:30	0.03 ± 0.01	43.06 ± 0.17	0.97 ± 0.01	1.4 ± 0.1	−7.8 ± 0.3
20/02 00:30 – 20/02 04:30	0.07 ± 0.01	43.51 ± 0.18	0.98 ± 0.01	0.7 ± 0.1	−9.7 ± 0.3
20/02 04:30 – 20/02 07:30	0.02 ± 0.01	43.78 ± 0.22	0.89 ± 0.01	4.7 ± 0.4	−8.6 ± 0.5
20/02 07:30 – 20/02 10:30	0.05 ± 0.01	43.92 ± 0.18	0.60 ± 0.02	17.6 ± 1.0	−10.4 ± 1.1
20/02 10:30 – 20/02 13:30	0.10 ± 0.02	43.06 ± 0.18	0.57 ± 0.02	18.4 ± 1.0	−6.1 ± 1.0
20/02 16:30 – 20/02 18:00	0.03 ± 0.01	39.97 ± 0.18	0.69 ± 0.02	12.3 ± 0.8	−5.3 ± 0.8

20/02 18:00 – 20/02 21:00	0.01 ± 0.01	41.75 ± 0.19	0.90 ± 0.01	4.3 ± 0.5	−7.9 ± 0.6
24/02 07:30 – 24/02 10:30	0.01 ± 0.01	43.21 ± 0.18	0.29 ± 0.02	30.7 ± 0.9	−11.9 ± 0.9
24/02 10:30 – 24/02 13:30	0.07 ± 0.01	41.95 ± 0.18	0.51 ± 0.02	20.6 ± 1.0	−4.1 ± 1.1
24/02 16:30 – 24/02 18:00	0.16 ± 0.03	39.80 ± 0.16	0.79 ± 0.02	8.4 ± 0.6	−7.2 ± 0.7
24/02 18:00 – 24/02 21:00	0.01 ± 0.01	40.88 ± 0.18	0.82 ± 0.02	7.2 ± 0.6	−7.3 ± 0.6
24/02 21:00 – 25/02 00:00	0.03 ± 0.02	42.20 ± 0.19	0.95 ± 0.01	2.1 ± 0.3	−7.3 ± 0.4
25/02 00:00 – 25/02 04:00	0.19 ± 0.03	42.48 ± 0.18	0.99 ± 0.01	0.3 ± 0.1	−10.3 ± 0.3
25/02 04:00 – 25/02 07:30	0.09 ± 0.01	42.69 ± 0.17	0.86 ± 0.02	5.8 ± 1.0	−7.3 ± 1.0
Mean	*0.06*	*42.31*	*0.77*	*9.6*	*−7.9*
Std dev	*0.06*	*1.32*	*0.21*	*9.1*	*2.0*

(1) Calculated from A^*_{day} between 7:30–18:00 LT and from A^*_{night} between 18:00–07:30 LT (A^*_{day} and A^*_{night} expressions are given in Section 2.4.2).
(2) Calculated from Eq. (10) for GP 1 and from Eq. (11) for GP 2
(3) Calculated from Eq. (9)

Table 3). A^*_{day} and A^*_{night} expressions are given in Section 2.4.2. Overall, during NO_2 sampling intervals, the A^* values are small (mean ± one standard deviation: 0.21 ± 0.51) and reflect an EIE-dominated regime with high NO_x (Li et al., 2020). It is interesting to note that the highest A^* values are observed between 13:30 and 16:30 LT, and correspond to the two data points in Figure 3 that lie outside the 95 % confidence interval of the regression line. These results suggest that EIE is the dominant N fractionation processes between NO_x and NO_2 during both day and night ($A^* < 0.46$), with the exception of mid-afternoon when LCIE competes with EIE ($A^* > 0.46$).

To quantify the overall N fractionation effect (F_N) between NO_x and NO_2, we dissociate the two samples collected between 13:30 and 16:30 LT into a different group (Group #1 = GP 1) from the other samples (Group #2 = GP 2). F_N of GP 1 and GP 2 is calculated using Eq. (10) (which combines LCIE and EIE regimes) and Eq. (11) (which considers only the EIE regime), respectively. Calculated F_N are reported in

Sampling interval (start – end)	A^*(1)	F_N(2)	f_{NO_2}	$\Delta^{15}(NO_2 - NO_x)$(3) /‰	$\delta^{15}N(NO_x)$ /‰
GP #1					
20/02 13:30 – 20/02 16:30	0.46 ± 0.08	25.00 ± 2.27	0.74 ± 0.02	6.5 ± 0.9	−7.2 ± 0.9
24/02 13:30 – 24/02 16:30	2.09 ± 0.39	6.90 ± 1.97	0.78 ± 0.02	1.5 ± 0.4	−6.9 ± 0.6
Mean	*1.27*	*16.39*	*0.76*	*4.1*	*−7.1*
Std dev	*1.14*	*12.58*	*0.03*	*3.5*	*0.2*
GP #2					
19/02 21:00 – 20/02 00:30	0.03 ± 0.01	43.06 ± 0.17	0.97 ± 0.01	1.4 ± 0.1	−7.8 ± 0.3
20/02 00:30 – 20/02 04:30	0.07 ± 0.01	43.51 ± 0.18	0.98 ± 0.01	0.7 ± 0.1	−9.7 ± 0.3
20/02 04:30 – 20/02 07:30	0.02 ± 0.01	43.78 ± 0.22	0.89 ± 0.01	4.7 ± 0.4	−8.6 ± 0.5
20/02 07:30 – 20/02 10:30	0.05 ± 0.01	43.92 ± 0.18	0.60 ± 0.02	17.6 ± 1.0	−10.4 ± 1.1
20/02 10:30 – 20/02 13:30	0.10 ± 0.02	43.06 ± 0.18	0.57 ± 0.02	18.4 ± 1.0	−6.1 ± 1.0
20/02 16:30 – 20/02 18:00	0.03 ± 0.01	39.97 ± 0.18	0.69 ± 0.02	12.3 ± 0.8	−5.3 ± 0.8

20/02 18:00 – 20/02 21:00	0.01 ± 0.01	41.75 ± 0.19	0.90 ± 0.01	4.3 ± 0.5	−7.9 ± 0.6
24/02 07:30 – 24/02 10:30	0.01 ± 0.01	43.21 ± 0.18	0.29 ± 0.02	30.7 ± 0.9	−11.9 ± 0.9
24/02 10:30 – 24/02 13:30	0.07 ± 0.01	41.95 ± 0.18	0.51 ± 0.02	20.6 ± 1.0	−4.1 ± 1.1
24/02 16:30 – 24/02 18:00	0.16 ± 0.03	39.80 ± 0.16	0.79 ± 0.02	8.4 ± 0.6	−7.2 ± 0.7
24/02 18:00 – 24/02 21:00	0.01 ± 0.01	40.88 ± 0.18	0.82 ± 0.02	7.2 ± 0.6	−7.3 ± 0.6
24/02 21:00 – 25/02 00:00	0.03 ± 0.02	42.20 ± 0.19	0.95 ± 0.01	2.1 ± 0.3	−7.3 ± 0.4
25/02 00:00 – 25/02 04:00	0.19 ± 0.03	42.48 ± 0.18	0.99 ± 0.01	0.3 ± 0.1	−10.3 ± 0.3
25/02 04:00 – 25/02 07:30	0.09 ± 0.01	42.69 ± 0.17	0.86 ± 0.02	5.8 ± 1.0	−7.3 ± 1.0
Mean	*0.06*	*42.31*	*0.77*	*9.6*	*−7.9*
Std dev	*0.06*	*1.32*	*0.21*	*9.1*	*2.0*

(1) Calculated from A^*_{day} between 7:30–18:00 LT and from A^*_{night} between 18:00–07:30 LT (A^*_{day} and A^*_{night} expressions are given in Section 2.4.2).
(2) Calculated from Eq. (10) for GP 1 and from Eq. (11) for GP 2
(3) Calculated from Eq. (9)

Table 3 and data used for calculations can be found in Section 2.4.2 and in the Supplement. Calculated F_N is significantly different between GP 1 and GP 2, with a mean of 16.4 ‰ and 42.3 ‰, respectively. The close match between the calculated average F_N of GP 2 and the observed F_N ((43.6 ± 3.3) ‰; slope of the regression line in Figure 3) provides strong evidence for the reliability of Eq. (11), as well as the expression of $\alpha_{EIE(NO_2/NO)}$ used therein, to accurately describe the N fractionation between NO_x emissions and NO_2 at our site, and hence, to describe most of the variability of $\delta^{15}N(NO_2)$ measurements. This result holds significant importance in confirming the theoretical N isotopic fractionation framework used in prior research studies. It is also important to stress the influence of LCIE effects for GP 1, highlighting the high dependency of $\delta^{15}N(NO_2)$ to local environmental conditions. According to the A^* factor, a greater influence of LCIE in mid-afternoon could have contributed to the outlying of the two samples collected between 13:30 and 16:30 LT (GP 1). However, as mentioned above, the sample collected on Feb 24 between 13:30 and 16:30 LT has a significant blank. Therefore, it cannot be confirmed with certainty that the reason this sample falls outside the 95 % confidence interval of the regression line is solely due to LCIE. Nevertheless, the overall conclusion that EIE dominates the variability of $\delta^{15}N(NO_2)$ at our site is not affected by this uncertainty.

The $\delta^{15}N$ shift in NO_2 relative to emitted NO_x ($\Delta^{15}(NO_2 - NO_x)$) is calculated for individual NO_2 sample using the mean ambient temperature during each sampling period. The mean atmospheric $\delta^{15}N$ of NO_x ($\delta^{15}N(NO_x)$) is then estimated by subtracting the $\Delta^{15}(NO_2 - NO_x)$ value from the observed $\delta^{15}N(NO_2)$ value. $\Delta^{15}(NO_2 - NO_x)$ and $\delta^{15}N(NO_x)$ estimates are reported in

Sampling interval (start – end)	$A^{*(1)}$	$F_N^{(2)}$	f_{NO_2}	$\Delta^{15}(NO_2 - NO_x)^{(3)}$ /‰	$\delta^{15}N(NO_x)$ /‰
GP #1					
20/02 13:30 – 20/02 16:30	0.46 ± 0.08	25.00 ± 2.27	0.74 ± 0.02	6.5 ± 0.9	−7.2 ± 0.9
24/02 13:30 – 24/02 16:30	2.09 ± 0.39	6.90 ± 1.97	0.78 ± 0.02	1.5 ± 0.4	−6.9 ± 0.6

Mean	*1.27*	*16.39*	*0.76*	*4.1*	*−7.1*
Std dev	*1.14*	*12.58*	*0.03*	*3.5*	*0.2*
GP #2					
19/02 21:00 – 20/02 00:30	0.03 ± 0.01	43.06 ± 0.17	0.97 ± 0.01	1.4 ± 0.1	−7.8 ± 0.3
20/02 00:30 – 20/02 04:30	0.07 ± 0.01	43.51 ± 0.18	0.98 ± 0.01	0.7 ± 0.1	−9.7 ± 0.3
20/02 04:30 – 20/02 07:30	0.02 ± 0.01	43.78 ± 0.22	0.89 ± 0.01	4.7 ± 0.4	−8.6 ± 0.5
20/02 07:30 – 20/02 10:30	0.05 ± 0.01	43.92 ± 0.18	0.60 ± 0.02	17.6 ± 1.0	−10.4 ± 1.1
20/02 10:30 – 20/02 13:30	0.10 ± 0.02	43.06 ± 0.18	0.57 ± 0.02	18.4 ± 1.0	−6.1 ± 1.0
20/02 16:30 – 20/02 18:00	0.03 ± 0.01	39.97 ± 0.18	0.69 ± 0.02	12.3 ± 0.8	−5.3 ± 0.8
20/02 18:00 – 20/02 21:00	0.01 ± 0.01	41.75 ± 0.19	0.90 ± 0.01	4.3 ± 0.5	−7.9 ± 0.6
24/02 07:30 – 24/02 10:30	0.01 ± 0.01	43.21 ± 0.18	0.29 ± 0.02	30.7 ± 0.9	−11.9 ± 0.9
24/02 10:30 – 24/02 13:30	0.07 ± 0.01	41.95 ± 0.18	0.51 ± 0.02	20.6 ± 1.0	−4.1 ± 1.1
24/02 16:30 – 24/02 18:00	0.16 ± 0.03	39.80 ± 0.16	0.79 ± 0.02	8.4 ± 0.6	−7.2 ± 0.7
24/02 18:00 – 24/02 21:00	0.01 ± 0.01	40.88 ± 0.18	0.82 ± 0.02	7.2 ± 0.6	−7.3 ± 0.6
24/02 21:00 – 25/02 00:00	0.03 ± 0.02	42.20 ± 0.19	0.95 ± 0.01	2.1 ± 0.3	−7.3 ± 0.4
25/02 00:00 – 25/02 04:00	0.19 ± 0.03	42.48 ± 0.18	0.99 ± 0.01	0.3 ± 0.1	−10.3 ± 0.3
25/02 04:00 – 25/02 07:30	0.09 ± 0.01	42.69 ± 0.17	0.86 ± 0.02	5.8 ± 1.0	−7.3 ± 1.0
Mean	*0.06*	*42.31*	*0.77*	*9.6*	*−7.9*
Std dev	*0.06*	*1.32*	*0.21*	*9.1*	*2.0*

(1) Calculated from A^*_{day} between 7:30–18:00 LT and from A^*_{night} between 18:00–07:30 LT (A^*_{day} and A^*_{night} expressions are given in Section 2.4.2).
(2) Calculated from Eq. (10) for GP 1 and from Eq. (11) for GP 2
(3) Calculated from Eq. (9)

Table 3. $\Delta^{15}(NO_2 - NO_x)$ varies greatly over the two sampling periods (from 0.7 ‰ to 30.7 ‰) with a mean value of ca. 9 ‰ (mean of GP #1 and GP #2). $\delta^{15}N(NO_x)$ show much less variability with an overall mean at (−7.8 ± 1.9) ‰ (mean of GP #1 and GP #2), in very good agreement with the value derived from the regression relationship (−8.8 ‰; intercept of the regression line in Figure 3). Therefore, there appears that there is little variation in NO_x emission sources at our site, and the wide variability in $\delta^{15}N(NO_2)$ is mainly driven by important equilibrium post-emission isotopic effects.

Sampling interval (start – end)	$A^{*(1)}$	$F_N^{(2)}$	f_{NO_2}	$\Delta^{15}(NO_2 - NO_x)^{(3)}$ /‰	$\delta^{15}N(NO_x)$ /‰
GP #1					
20/02 13:30 – 20/02 16:30	0.46 ± 0.08	25.00 ± 2.27	0.74 ± 0.02	6.5 ± 0.9	−7.2 ± 0.9
24/02 13:30 – 24/02 16:30	2.09 ± 0.39	6.90 ± 1.97	0.78 ± 0.02	1.5 ± 0.4	−6.9 ± 0.6
Mean	*1.27*	*16.39*	*0.76*	*4.1*	*−7.1*
Std dev	*1.14*	*12.58*	*0.03*	*3.5*	*0.2*
GP #2					
19/02 21:00 – 20/02 00:30	0.03 ± 0.01	43.06 ± 0.17	0.97 ± 0.01	1.4 ± 0.1	−7.8 ± 0.3
20/02 00:30 – 20/02 04:30	0.07 ± 0.01	43.51 ± 0.18	0.98 ± 0.01	0.7 ± 0.1	−9.7 ± 0.3
20/02 04:30 – 20/02 07:30	0.02 ± 0.01	43.78 ± 0.22	0.89 ± 0.01	4.7 ± 0.4	−8.6 ± 0.5
20/02 07:30 – 20/02 10:30	0.05 ± 0.01	43.92 ± 0.18	0.60 ± 0.02	17.6 ± 1.0	−10.4 ± 1.1
20/02 10:30 – 20/02 13:30	0.10 ± 0.02	43.06 ± 0.18	0.57 ± 0.02	18.4 ± 1.0	−6.1 ± 1.0
20/02 16:30 – 20/02 18:00	0.03 ± 0.01	39.97 ± 0.18	0.69 ± 0.02	12.3 ± 0.8	−5.3 ± 0.8
20/02 18:00 – 20/02 21:00	0.01 ± 0.01	41.75 ± 0.19	0.90 ± 0.01	4.3 ± 0.5	−7.9 ± 0.6
24/02 07:30 – 24/02 10:30	0.01 ± 0.01	43.21 ± 0.18	0.29 ± 0.02	30.7 ± 0.9	−11.9 ± 0.9
24/02 10:30 – 24/02 13:30	0.07 ± 0.01	41.95 ± 0.18	0.51 ± 0.02	20.6 ± 1.0	−4.1 ± 1.1
24/02 16:30 – 24/02 18:00	0.16 ± 0.03	39.80 ± 0.16	0.79 ± 0.02	8.4 ± 0.6	−7.2 ± 0.7
24/02 18:00 – 24/02 21:00	0.01 ± 0.01	40.88 ± 0.18	0.82 ± 0.02	7.2 ± 0.6	−7.3 ± 0.6
24/02 21:00 – 25/02 00:00	0.03 ± 0.02	42.20 ± 0.19	0.95 ± 0.01	2.1 ± 0.3	−7.3 ± 0.4
25/02 00:00 – 25/02 04:00	0.19 ± 0.03	42.48 ± 0.18	0.99 ± 0.01	0.3 ± 0.1	−10.3 ± 0.3
25/02 04:00 – 25/02 07:30	0.09 ± 0.01	42.69 ± 0.17	0.86 ± 0.02	5.8 ± 1.0	−7.3 ± 1.0
Mean	*0.06*	*42.31*	*0.77*	*9.6*	*−7.9*
Std dev	*0.06*	*1.32*	*0.21*	*9.1*	*2.0*

(1) Calculated from A^*_{day} between 7:30–18:00 LT and from A^*_{night} between 18:00–07:30 LT (A^*_{day} and A^*_{night} expressions are given in Section 2.4.2).
(2) Calculated from Eq. (10) for GP 1 and from Eq. (11) for GP 2
(3) Calculated from Eq. (9)

Table 3. Summary table of data used to estimate the N isotopic fractionation between NO_x emissions and NO_2 at our site ($\Delta(NO_2 - NO_x)$) and derive NO_x emissions δ^{15}N-fingerprint $\delta^{15}N(NO_x)$. The data reported are the mean values for each NO_2 sampling period (mean value ± absolute uncertainty).

3.4.2 NO_x emission sources derived from $\delta^{15}N(NO_2)$

To identify the main source of NO_x that contributes to the calculated $\delta^{15}N(NO_x)$ values at our site, Figure 4 displays the temporal variation of $\delta^{15}N(NO_x)$ obtained from individual NO_2 samples (dashed horizontal line) and the δ^{15}N range for different NO_x emission sources (coloured bands) such as for coal combustion ((19.5 ± 2.3) ‰ for power plant with selective catalytic reduction technology; Felix et al., 2012; Elliott et al., 2019), fossil gas combustion ((–16.5 ± 1.7) ‰; Walters et al., 2015), and fertilised soils ((–33.8 ± 12.2) ‰; Miller et al., 2018). δ^{15}N of NO_x released during biomass combustion is primarily driven by the δ^{15}N of the biomass burnt (Fibiger and Hastings, 2016). We estimate an average δ^{15}N of biomass combustion NO_x at (–0.1 ± 1.3) ‰, using the empirical relationship of Chai et al. (2019) (which was derived from

combustions of several North American wood species) and an average $\delta^{15}N$ of biomass at (–2.8 ± 2.0) ‰ representative of temperate forests (Martinelli et al., 1999). Regarding road traffic emissions, we have to stress that $\delta^{15}N$ values reported in the literature are rather variable mainly because N fractionations during the process of NO_x production can vary depending on the type of fuel used, the type of vehicle, the presence of an emission control system, and the time of commuting (Ammann et al., 1999; Felix and Elliott, 2014; Heaton, 1990; Miller et al., 2017; Walters et al., 2015b; Zong et al., 2020, 2017). We use here the mean vehicle-emitted $\delta^{15}N(NO_x)$ value given by Song et al. (2022) at (–7.1 ± 4.1) ‰, calculated from 181 measurements reported in the literature.

As previously noted, the values of estimated $\delta^{15}N(NO_x)$ show much less variability than $\delta^{15}N(NO_2)$, with no significant differences observed between daytime and nighttime values. The values of $\delta^{15}N(NO_x)$ range from −11.0 ‰ to −4.1 ‰, and despite the associated uncertainty, they are consistent with the $\delta^{15}N$ range of NO_x emissions from vehicle exhaust. The two sampling periods show similar $\delta^{15}N(NO_x)$ values with a slight diel variability. The estimated small variation in $\delta^{15}N(NO_x)$ throughout the day can be attributed to the temporal changes in the $\delta^{15}N$ signature of mobile NO_x sources. It has been shown that NO_x emitted by cold engines has a lower $\delta^{15}N$ signature compared to NO_x emitted from warm engines (Walters et al., 2015b). Hence, the early morning drop in $\delta^{15}N(NO_x)$ could be attributed to the influence of NO_x emitted from cold engines. As the day progresses, the time of commuting increases and therefore $\delta^{15}N(NO_x)$ tends to be less negative. Conversely, during the night, the slow $\delta^{15}N(NO_x)$ decline could be due to the replacement of NO_x from vehicle exhaust by NO_x emitted by fossil gas combustion, which is commonly used in Chamonix for home heating. Although biomass burning used for home heating would also tend to increase $\delta^{15}N(NO_x)$ during the day, it is unlikely to contribute more during the day than at night.

According to local NO_x emission inventories (Atmo-Auvergne-Rhône-Alpes, 2018; ORCAE, 2022), road transport is responsible of 64 % of NO_x emissions, ahead of heating oil and fossil gas combustion. Despite the consistency between our results and existing inventories, the significant variability in the $\delta^{15}N$ signature of NO_x emissions from vehicle exhaust precludes a reliable quantitative source apportionment of NO_x emissions from our estimated $\delta^{15}N(NO_x)$. Furthermore, the lack of information on the exact $\delta^{15}N$ signature of NO_x emitted from heating-oil combustion could also contribute to the potential bias of the emission source apportionment.

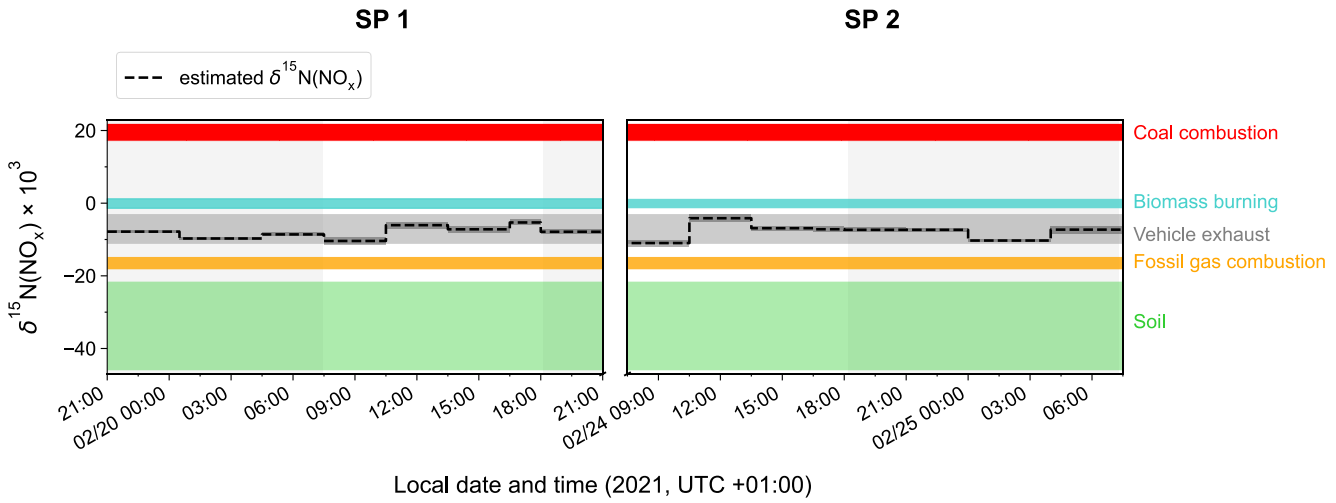

Figure 4. Time evolution of $\delta^{15}N(NO_x)$ (black dashed line) estimated from $\delta^{15}N(NO_2)$ observations in Chamonix after correction of N fractionation effects (length of horizontal line = sampling period, black shaded area = overall calculation error bar). Coloured shaded areas represent the standard deviation of the mean $\delta^{15}N$ value of individual NO_x emission source (coal combustion in red, biomass burning in blue, vehicle exhaust in grey, fossil gas in orange, and soil emissions in green). Grey backdrop shaded areas represent the nighttime (sunset to sunrise).

3.4.3 Interpretation of $\delta^{15}N(NO_3^-)$ observations

$\delta^{15}N(NO_3^-)$ also exhibits substantial variability during the day, ranging from −1.3 ‰ to 14.9 ‰ and from −4.2 ‰ to 9.7 ‰ during SP 1 and SP 2, respectively. At night, $\delta^{15}N(NO_3^-)$ is less variable, with an overall mean of (1.4 ± 1.2) ‰ and (−1.1 ± 0.4) ‰ during SP 1 and SP 2, respectively. $\delta^{15}N(NO_3^-)$ is within the range of observations reported in urban areas (He et al., 2020; Zhang et al., 2022a). A similar diurnal pattern was observed in samples collected during a cruise along the Californian coast in spring 2010 (Vicars et al., 2013), and isotopic exchanges between NO and NO_2 during the day were found to be the primary driver of the diel variability. In the previous section, we demonstrated that there is a significant ^{15}N partitioning between NO_x emissions and NO_2, the latter being enriched in ^{15}N compared to NO_x emissions. Interestingly, important enrichments in ^{15}N are also observed in NO_3^- .

As described above, at night during SP 1 and SP 2, $\delta^{15}N(NO_2)$ is close to $\delta^{15}N(NO_x)$ due to small N fractionation effects. However, between 18:00–7:30 LT, NO_3^- is enriched in ^{15}N relative to NO_2 by +6.3 ‰ and +1.4 ‰ in average during SP 1 and SP 2, respectively (**Erreur ! Source du renvoi introuvable.**). If we assume that, at night, NO_3^- is formed mainly by the conversion of surface NO_2 via the N_2O_5 pathway, then the difference between $\delta^{15}N(NO_3^-)$ and $\delta^{15}N(NO_2)$ ($\Delta^{15}(NO_3^- - NO_2)$) should reflect the N enrichment factor associated to this oxidation process. It is likely that an isotopic equilibrium is established between NO_2, NO_3, and N_2O_5, hence affecting the partitioning of ^{15}N between NO_2 and NO_3^- produced at night (Walters and Michalski, 2016). Neglecting KIE associated with the N_2O_5 pathway and using the expression of the EIE

fractionation factor between N_2O_5 and NO_2 given by Walters and Michalski (2015) (Appendix D) constrained with the mean nighttime temperature at our site, the isotopic composition of NO_3^- is expected be enriched in ^{15}N by about 29 ‰ compared to NO_2 . This estimated ^{15}N enrichment is about three times higher than the observed $\Delta^{15}(NO_3^- - NO_2)$ at our site. As daytime NO_3^- exhibits higher $\delta^{15}N$ values than during the night, it is not possible for daytime residuals at night to account for the lower than predicted fractionation effect between NO_2 and NO_3^-. These results highlight the importance of improving our understanding of the ^{15}N fractionation between NO_2 and NO_3^- associated with the N_2O_5 pathway. This could be achieved in an atmospheric simulation chamber that allows to reproduce individual processes in controlled conditions. The ^{15}N isotopic enrichment of NO_2 and NO_3^- collected from 7:30 to 18:00 LT shows a very contrasted distribution between SP 1 and SP 2, with a respective average $\Delta^{15}(NO_3^- - NO_2)$ of –0.4 ‰ and –10.0 ‰ (**Erreur ! Source du renvoi introuvable.**). Although subjected to significant uncertainties (Fan et al., 2019), the OH pathway is often associated to a KIE effect of −3 ‰ (Freyer, 1991), which is at odds with our observations. Similarly to the N_2O_5 pathway, there is an important need to better estimate the fractionation factor associated with the OH pathway.

There are significant differences in $\Delta^{15}(NO_3^- - NO_2)$ between SP 1 and SP 2, providing further evidence that NO_3^- collected during these two periods has undergone different formation processes and/or originate from different sources of NO_2. In addition, possible fractionation associated with phase change between HNO_3 and *p*-NO_3 during transport of Saharan dust could influence the $\delta^{15}N$ of collected NO_3^- during SP 2. However, given the lack of knowledge about N fractionation factors between NO_2 and NO_3^- and our limited dataset, we cannot conclude whether the changes in the distribution of NO_3^- isotopes during SP 2 result from changes in the phase distribution of NO_3^- or in NO_2 oxidation processes.

		$\delta^{15}N(NO_2)$ /‰	$\delta^{15}N(NO_3^-)$ /‰	$\delta^{15}N(NO_x)$ /‰	$\delta^{15}N(NO_3^- - NO_2)$ /‰
Daytime	SP 1	7.4 ± 4.7	7.0 ± 6.7	–9.9 ± 2.9	–0.4
(7:30-18:00)	SP 2	14.0 ± 13.9	4.0 ± 6.4	–10.8 ± 2.1	–10.0
Nighttime	SP 1	–5.1 ± 2.3	1.4 ± 1.2	–9.0 ± 0.8	6.3
(18:00-7:30)	SP 2	–2.5 ± 4.2	–1.1 ± 0.4	–9.9 ± 1.9	1.4

Table 4. Mean observed $\delta^{15}N$ data of NO_2 ($\delta^{15}N(NO_2)$) and NO_3^- ($\delta^{15}N(NO_3^-)$), calculated atmospheric $\delta^{15}N$ of NO_x ($\delta^{15}N(NO_x)$, and $\delta^{15}N$ shift between $\delta^{15}N(NO_3^-)$ and $\delta^{15}N(NO_2)$ ($\Delta^{15}(NO_3^- - NO_2)$).

4 Summary and implications

This study reports the first simultaneous measurements and analysis of $\Delta^{17}O$ and $\delta^{15}N$ in NO_2 and NO_3^-. The samplings were conducted at high temporal resolution (~ 3 h) in Chamonix, French Alps, over two distinct days in late February 2021., T~~t~~he

isotopic signals of both NO_2 and NO_3^- show substantial diurnal variabilities which are investigated in the light of local meteorological parameters and atmospheric observations (NO, NO_2, O_3, and PM).

The observed variability of $\Delta^{17}O(NO_2)$ can be well explained using $\Delta^{17}O$ mass balance equations and corroborates the analysis of previous observations carried out in Grenoble, French Alps, over a single day in spring (Albertin et al., 2021). On average, the high levels of NO_2 at our site are primarily driven by oxidation of local NO emissions by O_3. The observed diurnal variability in $\Delta^{17}O(NO_2)$ appears to be consistent with the diurnal variability expected in the $NO_x/O_3/RO_2$ chemistry with RO_2 levels of the order of pmol mol^{-1} which is in agreement with the range of direct winter RO_2 measurements reported in the literature. RO_2 is thought to contribute significantly to the formation of NO_2 in the early morning under high-NO_x conditions, which is in line with effective morning production of radical species reported in urban areas in winter. At night, $\Delta^{17}O(NO_2)$ reflects the nocturnal oxidation of surface NO emissions by O_3. These results provide additional evidence that $\Delta^{17}O(NO_2)$ measurements represent valuable constraints in the study of the reactive NO_x chemistry, down to the sub-daily temporal scales.

A clear linear relationship is found between $\delta^{15}N(NO_2)$ and the NO_2/NO_x ratio, indicating significant post-emission N fractionation effects. Theoretical N isotopic fractionation factors between NO and NO_2 at equilibrium and fractionation factors derived from the isotopic observations are found to be in good agreement, providing further support for the N isotopic fractionation theoretical framework commonly applied to the Leighton cycle. Observed $\delta^{15}N(NO_2)$ corrected for N fractionation effects allow to estimate the overall $\delta^{15}N$ signature of ambient NO_x at our site. Based on the existing $\delta^{15}N$-fingerprints of different NO_x emission sources, the main contribution at our site is very likely to be vehicle exhaust, which is confirmed by local emission inventories.

We use $\Delta^{17}O$ mass balance equations of NO_3^- constrained by observed $\Delta^{17}O(NO_2)$ to assess whether NO_3^- could originate locally from the oxidation of NO_2 at our site. During the first day of sampling, $\Delta^{17}O$ records of NO_2 and NO_3^- support the local oxidation of NO_2 to NO_3^- by OH radicals during the day, and via the heterogeneous hydrolysis of N_2O_5 during the night. The second day of sampling was affected by a Saharan dust event, accompanied by notable changes in the isotopic composition of NO_3^-. We propose that the formation of a surface inversion layer at night could have influenced the vertical distribution of $\Delta^{17}O(NO_2)$ and resulted in a positive gradient of $\Delta^{17}O(NO_3^-)$ with altitude, independently of the local NO_2 to NO_3^- conversion processes near the surface. In such scenario, the presence of Saharan dust could have promoted heterogeneous NO_2 oxidation leading to higher $\Delta^{17}O$ in NO_3^- formed aloft. The latter would have then mixed with the NO_3^- formed near the surface when the inversion breaks up during the day. Although still uncertain, the influence of the boundary layer dynamics on the distribution of $\Delta^{17}O$ in NO_3^- should be investigated in the future, notably for urban areas in winter.

The combined analysis of the first concurrent observations of $\delta^{15}N$ in NO_2 and NO_3^- highlights persistent uncertainties in the current estimates of the N fractionation factors associated with NO_2 and NO_3^- conversion processes. However, $\delta^{15}N(NO_3^-)$ records need to be corrected for N fractionation effects if they are to be used to trace back the $\delta^{15}N$ fingerprint of the primary NO_x emission sources. Detailed simulation chamber experiments could provide more kinetic data on the various N fractionation processes in order to better exploit $\delta^{15}N(NO_3^-)$ records to identify and quantify of the sources of reactive nitrogen.

The present thorough investigation of the $\Delta^{17}O$ and $\delta^{15}N$ in NO_2 and NO_3^- highlights (1) the potential to use sub-daily $\Delta^{17}O$ and $\delta^{15}N$ records to trace the sources and formation chemistry of NO_3^-, (2) the importance of measuring the NO_2 isotopic composition to avoid misinterpretation of NO_3^- isotopic records, and (3) the persistent knowledge gaps that prevent a complete assessment of the factors driving the variability in NO_3^- isotopic records. In most studies, the NO_3^- isotopic composition is interpreted on the basis of estimates of the isotopic composition of its precursor gases, assuming that both the chemistry of NO_2 (including its conversion to NO_3^-) and N isotopic fractionation effects are known. However, these assumptions are subject to very significant uncertainties, mainly in urban atmospheres. Hence, given the recent development of a method for measuring the multi-isotopic composition of NO_2, the accuracy and validity of the current interpretation framework of NO_3^- isotopic records should be tested in various environments. Such investigation can be performed by collecting simultaneously NO_2 and NO_3^-, as done here. We recommend to use this ~~approach~~ combined isotopic in order to avoid biased interpretations of NO_3^- isotopic records, particularly in urban areas during winter, and preferably at high temporal resolution (<24 h). In addition, the vertical distribution of NO_2 and NO_3^- isotopic composition should be documented in order to explore the possible role of the boundary layer dynamics in the variability of NO_2 and NO_3^- isotopic composition observed at the surface.

5 Appendix A: Reaction chemical rate

Reactions	Rate constants /cm^3 mol^{-1} s^{-1}	References
$NO + O_3 \rightarrow NO_2 + O_2$	$k_{NO+O_3} = 1.4 \times 10^{-12} \exp(-1310(K)/T)$	Atkinson et al. (2004)
$NO + RO_2 \rightarrow NO_2 + RO$	$k_{NO+RO_2} = 2.3 \times 10^{-12} \exp(360(K)//T)$	Atkinson et al. (2006)
$NO_2 + O_3 \xrightarrow{M} NO_3 + O_2$	$k_{NO_2+O_3} = 1.4 \times 10^{-13} \exp(-2470(K)//T)$	Atkinson et al. (2004)
$^{15}NO_2 + {}^{14}NO \rightarrow {}^{14}NO_2 + {}^{15}NO$	$k_{NO+NO_2} = 8.14 \times 10^{-14}$	Sharma et al. (1970)

Table A1. Kinetic constants used in this study.

6 Appendix B: Atmospheric lifetime of NO_2 and NO_3^-

	τ_{NO_2} (1)	$\tau_{NO_3^-}$ (2)	$k_{d(NO_2)}$ (s^{-1})	$k_{d(NO_3^-)}$ (s^{-1})
Day	5.1 min	27.8 h	0.5×10^{-5}	1.0×10^{-5}
Night	10.0 h	5.6 h	2.5×10^{-5}	5.0×10^{-5}

(1) Atmospheric lifetime relative to photolysis during the day (dry deposition and reaction NO_2 + OH are negligible) and to dry deposition and oxidation via O_3 during the night.

(2) Atmospheric lifetime relative to dry deposition

The boundary layer is fixed at 500 m during the day and at 100 m during the night. Dry deposition velocity (V_d) is fixed at 0.25 cm s^{-1} and 0.50 cm s^{-1} for NO_2 and NO_3^-, respectively (Holland et al., 1999; Zhang et al., 2009).

Table B1. Mean daytime (07:30–18:00 LT) and nighttime (18:00–07:30 LT) atmospheric lifetime of NO_2 (τ_{NO_2}) and NO_3^- ($\tau_{NO_3^-}$) and dry deposition constant ($k_d = V_d \times BLH$ where V_d is the dry deposition velocity and BLH is the boundary layer height).

7 Appendix C: Schematic of the N reactive cycle and associated $\Delta^{17}O$ transfers and N enrichment factors

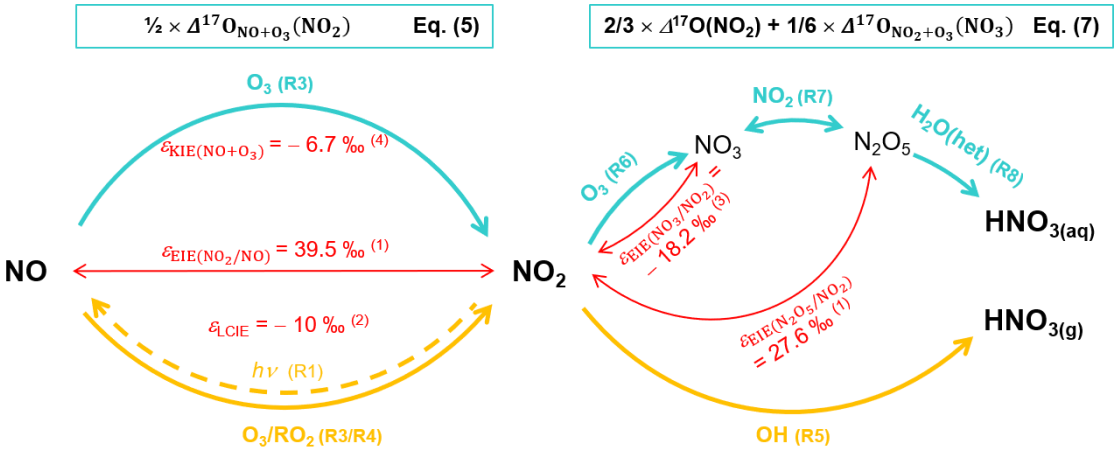

(1) Calculated at 298 K (Walters and Michalski, 2015)
(2) Experimental study at 298 K (Li et al., 2020)
(3) Calculated at 298 K (Walters et al., 2016)
(4) Calculated at 298 K (Fang et al., 2021)

Figure C1. Adapted from Elliott et al., (2019). Sketch of dominant daytime (thick yellow arrows) and nighttime (thick cyan arrows) NO_x to NO_3^- conversion processes and associated quantified N fractionation effects at 298 K (thin red arrows and text) and $\Delta^{17}O$ transfers (yellow and cyan boxes)

8 Appendix D: Equilibrium N fractionation factors

$$(\alpha_{EIE(X/Y)} - 1) \times 1000 = \frac{A}{T^4} \times 10^{10} + \frac{B}{T^3} \times 10^8 + \frac{C}{T^2} \times 10^6 + \frac{D}{T} \times 10^4$$

X/Y	A	B	C	D
NO_2/NO	3.847	–7.680	6.003	–0.118
N_2O_5/NO_2	1.004	–2.525	2.718	0.135

$$(\alpha_{KIE(X+Y)} - 1) \times 1000 = A \times \exp(B/T)$$

X + Y	A	B
$NO + O_3$	0.982	3.352

Table D1. Calculated regression coefficients for the N isotope exchange between NO_2/NO and N_2O_5/NO_2 over the temperature range of 150 to 450 K (Walters and Michalski, 2015) and for the N kinetic fractionation for the reaction $NO + O_3$ over the temperature range of 220 to 320 K (Fang et al., 2021).

9 Data availability

Data presented in this article are included in the Supplement.

10 Author contributions.

Grants obtained by KL and JS funded the project. AB, RB, QF, and IV performed the calibration of IBBCEAS and OFCEAS instruments, data acquisition and post-processing. SA conducted the sampling and laboratory analysis. NC provided technical support for isotopic mass spectrometry analysis. The study was designed as part of SA's PhD thesis supervised by SB and JS. The paper was written by SA under the supervision of JS and SB and contributions from all co-authors.

11 Competing interests.

The authors declare that they have no conflict of interest.

12 Acknowledgements.

This work benefited from CNRS and IGE infrastructures and laboratory platforms. The authors acknowledge the support of the CASPA program (Climate-relevant Aerosol Sources and Processes in the Arctic). The authors gratefully acknowledge Catherine Coulaud for providing temperature data in Chamonix, Jean-Luc Jaffrezo for providing data of previous filter measurements in Chamonix, and Anthony Lemoine, Matthieu Lafaysse and Louis Le Toumelin for providing S2M reanalysis and meteorological data. The authors particularly thanks Patrick Ginot, Anthony Vella, Armelle Crouzet, and Bruno Jourdain for instrumental and laboratory technical support. Finally, the authors thank Alexis Lamothe for assistance during the sampling campaign and Pete Akers for his thorough proofreading of the manuscript and his constructive comments.

13 Financial support.

This research has been supported by the Agence Nationale de la Recherche (ANR) via contract ANR-21-CE01-0017 CASPA and INSU-CNRS (National Institute of Sciences of the Universe) via its national LEFE program (Les Enveloppes Fluides et l'Environnement) and by a grant from Labex OSUG@2020 (Investissements d'avenir – ANR10 LABX56) and IDEX-UGA ANR project ANR-15-IDEX-02.

14 References

Albertin, S., Savarino, J., Bekki, S., Barbero, A., and Caillon, N.: Measurement report: Nitrogen isotopes ($\delta^{15}N$) and first quantification of oxygen isotope anomalies ($\Delta^{17}O$, $\delta^{18}O$) in atmospheric nitrogen dioxide, Atmospheric Chemistry and Physics, 21, 10477–10497, https://doi.org/10.5194/acp-21-10477-2021, 2021.

Alexander, B., Hastings, M. G., Allman, D. J., Dachs, J., Thornton, J. A., and Kunasek, S. A.: Quantifying atmospheric nitrate formation pathways based on a global model of the oxygen isotopic composition ($\Delta^{17}O$) of atmospheric nitrate, Atmospheric Chemistry and Physics, 9, 5043–5056, https://doi.org/10.5194/acp-9-5043-2009, 2009.

Alexander, B., Sherwen, T., Holmes, C. D., Fisher, J. A., Chen, Q., Evans, M. J., and Kasibhatla, P.: Global inorganic nitrate production mechanisms: comparison of a global model with nitrate isotope observations, Atmospheric Chemistry and Physics, 20, 3859–3877, https://doi.org/10.5194/acp-20-3859-2020, 2020.

Alicke, B., Geyer, A., Hofzumahaus, A., Holland, F., Konrad, S., Pätz, H. W., Schäfer, J., Stutz, J., Volz-Thomas, A., and Platt, U.: OH formation by HONO photolysis during the BERLIOZ experiment, Journal of Geophysical Research: Atmospheres, 108, PHO 3-1-PHO 3-17, https://doi.org/10.1029/2001JD000579, 2003.

Allard, J.: Qualité de l'air dans la Vallée de l'Arve : météorologie locale et mesures des réductions des émissions liées au chauffage au bois, PhD Thesis, Université Grenoble Alpes, 2018.

Ammann, M., Siegwolf, R., Pichlmayer, F., Suter, M., Saurer, M., and Brunold, C.: Estimating the uptake of trafic-derived NO_2 from ^{15}N abundance in Norway spruce needles, Oecologia, 118, 124–131, https://doi.org/10.1007/s004420050710, 1999.

Angelisi, M. D. and Gaudichet, A.: Saharan dust deposition over Mont Blanc (French Alps) during the last 30 years, Tellus B, 43, 61–75, https://doi.org/10.1034/j.1600-0889.1991.00005.x, 1991.

Appel, B. R., Wall, S. M., Tokiwa, Y., and Haik, M.: Simultaneous nitric acid, particulate nitrate and acidity measurements in ambient air, Atmospheric Environment, 14, 549–554, https://doi.org/10.1016/0004-6981(80)90084-0, 1980.

Appel, B. R., Tokiwa, Y., and Haik, M.: Sampling of nitrates in ambient air, Atmospheric Environment, 15, 283–289, https://doi.org/10.1016/0004-6981(81)90029-9, 1981.

Atkinson, R., Baulch, D. L., Cox, R. A., Crowley, J. N., Hampson, R. F., Hynes, R. G., Jenkin, M. E., Rossi, M. J., and Troe, J.: Evaluated kinetic and photochemical data for atmospheric chemistry: Volume I - gas phase reactions of O_x, HO_x, NO_x and SO_x species, Atmospheric Chemistry and Physics, 4, 1461–1738, https://doi.org/10.5194/acp-4-1461-2004, 2004.

Atkinson, R., Baulch, D. L., Cox, R. A., Crowley, J. N., Hampson, R. F., Hynes, R. G., Jenkin, M. E., Rossi, M. J., Troe, J., and IUPAC Subcommittee: Evaluated kinetic and photochemical data for atmospheric chemistry: Volume II - gas phase reactions of organic species, Atmospheric Chemistry and Physics, 6, 3625–4055, https://doi.org/10.5194/acp-6-3625-2006, 2006.

Atmo-Auvergne-Rhône-Alpes: Bilan des connaissances sur la qualité de l'air dans la vallée de l'Arve, Atmo-Auvergne-Rhône-Alpes, https://www.atmo-auvergnerhonealpes.fr/publications/bilan-des-connaissances-sur-la-qualite-de-lair-dans-la-vallee-de-larve, 2018.

Aumont, B., Chervier, F., and Laval, S.: Contribution of HONO sources to the NOx/HOx/O3 chemistry in the polluted boundary layer, Atmospheric Environment, 37, 487–498, https://doi.org/10.1016/S1352-2310(02)00920-2, 2003.

Aymoz, G., Jaffrezo, J.-L., Jacob, V., Colomb, A., and George, C.: Evolution of organic and inorganic components of aerosol during a Saharan dust episode observed in the French Alps, Atmospheric Chemistry and Physics, 4, 2499–2512, https://doi.org/10.5194/acp-4-2499-2004, 2004.

Aymoz, G., Jaffrezo, J. L., Chapuis, D., Cozic, J., and Maenhaut, W.: Seasonal variation of PM_{10} main constituents in two valleys of the French Alps. I: EC/OC fractions, Atmospheric Chemistry and Physics, 7, 661–675, https://doi.org/10.5194/acp-7-661-2007, 2007.

Barbero, A., Blouzon, C., Savarino, J., Caillon, N., Dommergue, A., and Grilli, R.: A compact incoherent broadband cavity-enhanced absorption spectrometer for trace detection of nitrogen oxides, iodine oxide and glyoxal at levels below parts per billion for field applications, Atmospheric Measurement Techniques, 13, 4317–4331, https://doi.org/10.5194/amt-13-4317-2020, 2020.

Barkan, E. and Luz, B.: High-precision measurements of $^{17}O/^{16}O$ and $^{18}O/^{16}O$ of O_2 and O_2/Ar ratio in air, Rapid Commun. Mass Spectrom., 17, 2809–2814, https://doi.org/10.1002/rcm.1267, 2003.

Bauer, S. E., Koch, D., Unger, N., Metzger, S. M., Shindell, D. T., and Streets, D. G.: Nitrate aerosols today and in 2030: a global simulation including aerosols and tropospheric ozone, Atmos. Chem. Phys., 7, 5043–5059, https://doi.org/10.5194/acp-7-5043-2007, 2007.

Bekker, C., Walters, W. W., Murray, L. T., and Hastings, M. G.: Nitrate chemistry in the northeast US – Part 1: Nitrogen isotope seasonality tracks nitrate formation chemistry, Atmospheric Chemistry and Physics, 23, 4185–4201, https://doi.org/10.5194/acp-23-4185-2023, 2023.

Berhanu, T. A., Savarino, J., Bhattacharya, S. K., and Vicars, W. C.: ^{17}O excess transfer during the $NO_2 + O_3 \rightarrow NO_3 + O_2$ reaction, The Journal of Chemical Physics, 136, 044311, https://doi.org/10.1063/1.3666852, 2012.

Brown, S. S.: Variability in Nocturnal Nitrogen Oxide Processing and Its Role in Regional Air Quality, Science, 311, 67–70, https://doi.org/10.1126/science.1120120, 2006.

Brown, S. S. and Stutz, J.: Nighttime radical observations and chemistry, Chem Soc Rev, 41, 6405–6447, https://doi.org/10.1039/c2cs35181a, 2012.

Brown, S. S., Dubé, W. P., Peischl, J., Ryerson, T. B., Atlas, E., Warneke, C., de Gouw, J. A., te Lintel Hekkert, S., Brock, C. A., Flocke, F., Trainer, M., Parrish, D. D., Feshenfeld, F. C., and Ravishankara, A. R.: Budgets for nocturnal VOC oxidation by nitrate radicals aloft during the 2006 Texas Air Quality Study, Journal of Geophysical Research: Atmospheres, 116, https://doi.org/10.1029/2011JD016544, 2011.

Brulfert, G., Chemel, C., Chaxel, E., and Chollet, J. P.: Modelling photochemistry in alpine valleys, Atmos. Chem. Phys., https://doi.org/10.5194/acp-5-2341-2005, 2005.

Casciotti, K. L., Sigman, D. M., Hastings, M. G., Böhlke, J. K., and Hilkert, A.: Measurement of the oxygen isotopic composition of nitrate in seawater and freshwater using the denitrifier method, Analytical Chemistry, 74, 4905–4912, https://doi.org/10.1021/ac020113w, 2002.

Chan, Y.-C., Evans, M. J., He, P., Holmes, C. D., Jaeglé, L., Kasibhatla, P., Liu, X.-Y., Sherwen, T., Thornton, J. A., Wang, X., Xie, Z., Zhai, S., and Alexander, B.: Heterogeneous Nitrate Production Mechanisms in Intense Haze Events in the North China Plain, Journal of Geophysical Research: Atmospheres, 126, e2021JD034688, https://doi.org/10.1029/2021JD034688, 2021.

Chang, Y., Zhang, Y., Tian, C., Zhang, S., Ma, X., Cao, F., Liu, X., Zhang, W., Kuhn, T., and Lehmann, M. F.: Nitrogen isotope fractionation during gas-to-particle conversion of NO_x to NO_3^- in the atmosphere – implications for isotope-based NO_x source apportionment, Atmospheric Chemistry and Physics, 18, 11647–11661, https://doi.org/10.5194/acp-18-11647-2018, 2018.

Chazette, P., Couvert, P., Randriamiarisoa, H., Sanak, J., Bonsang, B., Moral, P., Berthier, S., Salanave, S., and Toussaint, F.: Three-dimensional survey of pollution during winter in French Alps valleys, Atmospheric Environment, 39, 1035–1047, https://doi.org/10.1016/j.atmosenv.2004.10.014, 2005.

Crutzen, P. J.: The Role of NO and NO_2 in the Chemistry of the Troposphere and Stratosphere, Annu. Rev. Earth Planet. Sci., 7, 443–472, https://doi.org/10.1146/annurev.ea.07.050179.002303, 1979.

Delmas, R. J.: Snow chemistry of high altitude glaciers in the French Alps, 46, 304, https://doi.org/10.3402/tellusb.v46i4.15806, 1994.

Dentener, F. J. and Crutzen, P. J.: Reaction of N2O5 on tropospheric aerosols: Impact on the global distributions of NO x , O3, and OH, Journal of Geophysical Research: Atmospheres, 98, 7149–7163, https://doi.org/10.1029/92JD02979, 1993.

Di Mauro, B., Garzonio, R., Rossini, M., Filippa, G., Pogliotti, P., Galvagno, M., Morra di Cella, U., Migliavacca, M., Baccolo, G., Clemenza, M., Delmonte, B., Maggi, V., Dumont, M., Tuzet, F., Lafaysse, M., Morin, S., Cremonese, E., and Colombo, R.: Saharan dust events in the European Alps: role in snowmelt and geochemical characterization, The Cryosphere, 13, 1147–1165, https://doi.org/10.5194/tc-13-1147-2019, 2019.

Dubey, M. K., Mohrschladt, R., Donahue, N. M., and Anderson, J. G.: Isotope Specific Kinetics of Hydroxyl Radical (OH) with Water (H_2O): Testing Models of Reactivity and Atmospheric Fractionation, J. Phys. Chem. A, 101, 1494–1500, https://doi.org/10.1021/jp962332p, 1997.

Edwards, P. M., Brown, S. S., Roberts, J. M., Ahmadov, R., Banta, R. M., deGouw, J. A., Dubé, W. P., Field, R. A., Flynn, J. H., Gilman, J. B., Graus, M., Helmig, D., Koss, A., Langford, A. O., Lefer, B. L., Lerner, B. M., Li, R., Li, S.-M., McKeen, S. A., Murphy, S. M., Parrish, D. D., Senff, C. J., Soltis, J., Stutz, J., Sweeney, C., Thompson, C. R., Trainer, M. K., Tsai, C., Veres, P. R., Washenfelder, R. A., Warneke, C., Wild, R. J., Young, C. J., Yuan, B., and Zamora, R.: High winter ozone pollution from carbonyl photolysis in an oil and gas basin, Nature, 514, 351–354, https://doi.org/10.1038/nature13767, 2014.

Elliott, E. M., Yu, Z., Cole, A. S., and Coughlin, J. G.: Isotopic advances in understanding reactive nitrogen deposition and atmospheric processing, Science of The Total Environment, 662, 393–403, https://doi.org/10.1016/j.scitotenv.2018.12.177, 2019.

Emmerson, K. M., Carslaw, N., Carpenter, L. J., Heard, D. E., Lee, J. D., and Pilling, M. J.: Urban Atmospheric Chemistry During the PUMA Campaign 1: Comparison of Modelled OH and HO_2 Concentrations with Measurements, J Atmos Chem, 52, 143–164, https://doi.org/10.1007/s10874-005-1322-3, 2005.

Fan, M.-Y., Zhang, Y.-L., Lin, Y.-C., Chang, Y.-H., Cao, F., Zhang, W.-Q., Hu, Y.-B., Bao, M.-Y., Liu, X.-Y., Zhai, X.-Y., Lin, X., Zhao, Z.-Y., and Song, W.-H.: Isotope-based source apportionment of nitrogen-containing aerosols: A case study in an industrial city in China, Atmospheric Environment, 212, 96–105, https://doi.org/10.1016/j.atmosenv.2019.05.020, 2019.

Fan, M.-Y., Zhang, Y.-L., Lin, Y.-C., Hong, Y., Zhao, Z.-Y., Xie, F., Du, W., Cao, F., Sun, Y., and Fu, P.: Important Role of NO_3 Radical to Nitrate Formation Aloft in Urban Beijing: Insights from Triple Oxygen Isotopes Measured at the Tower, Environ. Sci. Technol., 56, 6870–6879, https://doi.org/10.1021/acs.est.1c02843, 2022.

Fan, M.-Y., Zhang, W., Zhang, Y.-L., Li, J., Fang, H., Cao, F., Yan, M., Hong, Y., Guo, H., and Michalski, G.: Formation Mechanisms and Source Apportionments of Nitrate Aerosols in a Megacity of Eastern China Based On Multiple Isotope Observations, Journal of Geophysical Research: Atmospheres, 128, e2022JD038129, https://doi.org/10.1029/2022JD038129, 2023.

Fang, H., Walters, W. W., Mase, D., and Michalski, G.: i_NRACM: incorporating ^{15}N into the Regional Atmospheric Chemistry Mechanism (RACM) for assessing the role photochemistry plays in controlling the isotopic composition of NO_x, NO_y, and atmospheric nitrate, Geoscientific Model Development, 14, 5001–5022, https://doi.org/10.5194/gmd-14-5001-2021, 2021.

Felix, J. D. and Elliott, E. M.: Isotopic composition of passively collected nitrogen dioxide emissions: Vehicle, soil and livestock source signatures, Atmospheric Environment, 92, 359–366, https://doi.org/10.1016/j.atmosenv.2014.04.005, 2014.

Felix, J. D., Elliott, E. M., and Shaw, S. L.: Nitrogen Isotopic Composition of Coal-Fired Power Plant NO_x: Influence of Emission Controls and Implications for Global Emission Inventories, Environ. Sci. Technol., 46, 3528–3535, https://doi.org/10.1021/es203355v, 2012.

Fibiger, D. L. and Hastings, M. G.: First Measurements of the Nitrogen Isotopic Composition of NO_x from Biomass Burning, Environ. Sci. Technol., 50, 11569–11574, https://doi.org/10.1021/acs.est.6b03510, 2016.

Finlayson-Pitts, B. J. and Pitts, J. N.: Chemistry of the Upper and Lower Atmosphere, Elsevier, https://doi.org/10.1016/B978-012257060-5/50003-4, 2000.

Frey, M. M., Savarino, J., Morin, S., Erbland, J., and Martins, J. M. F.: Photolysis imprint in the nitrate stable isotope signal in snow and atmosphere of East Antarctica and implications for reactive nitrogen cycling, Atmospheric Chemistry and Physics, 9, 8681–8696, https://doi.org/10.5194/acp-9-8681-2009, 2009.

Freyer, H. D.: Seasonal variation of $^{15}N/^{14}N$ ratios in atmospheric nitrate species, Tellus B, 43, 30–44, https://doi.org/10.1034/j.1600-0889.1991.00003.x, 1991.

Freyer, H. D., Kley, D., Volz-Thomas, A., and Kobel, K.: On the interaction of isotopic exchange processes with photochemical reactions in atmospheric oxides of nitrogen, Journal of Geophysical Research: Atmospheres, 98, 14791–14796, https://doi.org/10.1029/93JD00874, 1993.

Fu, X., Wang, T., Gao, J., Wang, P., Liu, Y., Wang, S., Zhao, B., and Xue, L.: Persistent Heavy Winter Nitrate Pollution Driven by Increased Photochemical Oxidants in Northern China, Environ. Sci. Technol., 54, 3881–3889, https://doi.org/10.1021/acs.est.9b07248, 2020.

Galeazzo, T., Bekki, S., Martin, E., Savarino, J., and Arnold, S. R.: Photochemical box modelling of volcanic SO_2 oxidation: isotopic constraints, Atmospheric Chemistry and Physics, 18, 17909–17931, https://doi.org/10.5194/acp-18-17909-2018, 2018.

Galloway, J. N., Townsend, A. R., Erisman, J. W., Bekunda, M., Cai, Z., Freney, J. R., Martinelli, L. A., Seitzinger, S. P., and Sutton, M. A.: Transformation of the Nitrogen Cycle: Recent Trends, Questions, and Potential Solutions, Science, 320, 889–892, https://doi.org/10.1126/science.1136674, 2008.

Gaudel, A., Cooper, O. R., Ancellet, G., Barret, B., Boynard, A., Burrows, J. P., Clerbaux, C., Coheur, P.-F., Cuesta, J., Cuevas, E., Doniki, S., Dufour, G., Ebojie, F., Foret, G., Garcia, O., Granados-Muñoz, M. J., Hannigan, J. W., Hase, F., Hassler, B., Huang, G., Hurtmans, D., Jaffe, D., Jones, N., Kalabokas, P., Kerridge, B., Kulawik, S., Latter, B., Leblanc, T., Le Flochmoën, E., Lin, W., Liu, J., Liu, X., Mahieu, E., McClure-Begley, A., Neu, J. L., Osman, M., Palm, M., Petetin, H.,

Petropavlovskikh, I., Querel, R., Rahpoe, N., Rozanov, A., Schultz, M. G., Schwab, J., Siddans, R., Smale, D., Steinbacher, M., Tanimoto, H., Tarasick, D. W., Thouret, V., Thompson, A. M., Trickl, T., Weatherhead, E., Wespes, C., Worden, H. M., Vigouroux, C., Xu, X., Zeng, G., and Ziemke, J.: Tropospheric Ozone Assessment Report: Present-day distribution and trends of tropospheric ozone relevant to climate and global atmospheric chemistry model evaluation, Elementa: Science of the Anthropocene, 6, https://doi.org/10.1525/elementa.291, 2018.

Geng, L., Alexander, B., Cole-Dai, J., Steig, E. J., Savarino, J., Sofen, E. D., and Schauer, A. J.: Nitrogen isotopes in ice core nitrate linked to anthropogenic atmospheric acidity change, Proc. Natl. Acad. Sci. U.S.A., 111, 5808–5812, https://doi.org/10.1073/pnas.1319441111, 2014.

Goudie, A. S. and Middleton, N. J.: Saharan dust storms: nature and consequences, Earth-Science Reviews, 56, 179–204, https://doi.org/10.1016/S0012-8252(01)00067-8, 2001.

Grannas, A. M., Jones, A. E., Dibb, J., Ammann, M., Anastasio, C., Beine, H. J., Bergin, M., Bottenheim, J., Boxe, C. S., Carver, G., Chen, G., Crawford, J. H., Dominé, F., Frey, M. M., Guzmán, M. I., Heard, D. E., Helmig, D., Hoffmann, M. R., Honrath, R. E., Huey, L. G., Hutterli, M., Jacobi, H. W., Klán, P., Lefer, B., McConnell, J., Plane, J., Sander, R., Savarino, J., Shepson, P. B., Simpson, W. R., Sodeau, J. R., von Glasow, R., Weller, R., Wolff, E. W., and Zhu, T.: An overview of snow photochemistry: evidence, mechanisms and impacts, Atmospheric Chemistry and Physics, 7, 4329–4373, https://doi.org/10.5194/acp-7-4329-2007, 2007.

Greilinger, M., Schauer, G., Baumann-Stanzer, K., Skomorowski, P., Schöner, W., and Kasper-Giebl, A.: Contribution of Saharan Dust to Ion Deposition Loads of High Alpine Snow Packs in Austria (1987–2017), Frontiers in Earth Science, 6, 2018.

Gu, P., Dallmann, T. R., Li, H. Z., Tan, Y., and Presto, A. A.: Quantifying Urban Spatial Variations of Anthropogenic VOC Concentrations and Source Contributions with a Mobile Sampling Platform, Int J Environ Res Public Health, 16, https://doi.org/10.3390/ijerph16091632, 2019.

He, P., Xie, Z., Chi, X., Yu, X., Fan, S., Kang, H., Liu, C., and Zhan, H.: Atmospheric $\Delta^{17}O(NO_3^-)$ reveals nocturnal chemistry dominates nitrate production in Beijing haze, Atmospheric Chemistry and Physics, 18, 14465–14476, https://doi.org/10.5194/acp-18-14465-2018, 2018.

He, P., Xie, Z., Yu, X., Wang, L., Kang, H., and Yue, F.: The observation of isotopic compositions of atmospheric nitrate in Shanghai China and its implication for reactive nitrogen chemistry, Science of The Total Environment, 714, 136727, https://doi.org/10.1016/j.scitotenv.2020.136727, 2020.

Heaton, T. H. E.: $^{15}N/^{14}N$ ratios of NO_x from vehicle engines and coal-fired power stations, Tellus B, 42, 304–307, https://doi.org/10.1034/j.1600-0889.1990.00007.x-i1, 1990.

Hoesly, R. M., Smith, S. J., Feng, L., Klimont, Z., Janssens-Maenhout, G., Pitkanen, T., Seibert, J. J., Vu, L., Andres, R. J., Bolt, R. M., Bond, T. C., Dawidowski, L., Kholod, N., Kurokawa, J., Li, M., Liu, L., Lu, Z., Moura, M. C. P., O'Rourke, P. R., and Zhang, Q.: Historical (1750–2014) anthropogenic emissions of reactive gases and aerosols from the Community Emissions Data System (CEDS), Geoscientific Model Development, 11, 369–408, https://doi.org/10.5194/gmd-11-369-2018, 2018.

Holland, E. A., Dentener, F. J., Braswell, B. H., and Sulzman, J. M.: Contemporary and pre-industrial global reactive nitrogen budgets, Biogeochemistry, 46, 7–43, https://doi.org/10.1023/A:1006148011944, 1999.

Huang, R.-J., Zhang, Y., Bozzetti, C., Ho, K.-F., Cao, J.-J., Han, Y., Daellenbach, K. R., Slowik, J. G., Platt, S. M., Canonaco, F., Zotter, P., Wolf, R., Pieber, S. M., Bruns, E. A., Crippa, M., Ciarelli, G., Piazzalunga, A., Schwikowski, M.,

Abbaszade, G., Schnelle-Kreis, J., Zimmermann, R., An, Z., Szidat, S., Baltensperger, U., Haddad, I. E., and Prévôt, A. S. H.: High secondary aerosol contribution to particulate pollution during haze events in China, Nature, 514, 218–222, https://doi.org/10.1038/nature13774, 2014.

Kaiser, J., Hastings, M. G., Houlton, B. Z., Röckmann, T., and Sigman, D. M.: Triple oxygen isotope analysis of nitrate using the denitrifier method and thermal decomposition of N_2O, Anal. Chem., 79, 599–607, https://doi.org/10.1021/ac061022s, 2007.

Kanaya, Y., Cao, R., Akimoto, H., Fukuda, M., Komazaki, Y., Yokouchi, Y., Koike, M., Tanimoto, H., Takegawa, N., and Kondo, Y.: Urban photochemistry in central Tokyo: 1. Observed and modeled OH and HO_2 radical concentrations during the winter and summer of 2004, Journal of Geophysical Research: Atmospheres, 112, https://doi.org/10.1029/2007JD008670, 2007.

Karydis, V. A., Tsimpidi, A. P., Pozzer, A., Astitha, M., and Lelieveld, J.: Effects of mineral dust on global atmospheric nitrate concentrations, Atmospheric Chemistry and Physics, 16, 1491–1509, https://doi.org/10.5194/acp-16-1491-2016, 2016.

Kim, H., Walters, W. W., Bekker, C., Murray, L. T., and Hastings, M. G.: Nitrate chemistry in the northeast US – Part 2: Oxygen isotopes reveal differences in particulate and gas-phase formation, Atmospheric Chemistry and Physics, 23, 4203–4219, https://doi.org/10.5194/acp-23-4203-2023, 2023.

Kirchstetter, T. W., Harley, R. A., and Littlejohn, D.: Measurement of Nitrous Acid in Motor Vehicle Exhaust, Environ. Sci. Technol., 30, 2843–2849, https://doi.org/10.1021/es960135y, 1996.

Kurtenbach, R., Becker, K. H., Gomes, J. A. G., Kleffmann, J., Lörzer, J. C., Spittler, M., Wiesen, P., Ackermann, R., Geyer, A., and Platt, U.: Investigations of emissions and heterogeneous formation of HONO in a road traffic tunnel, Atmospheric Environment, 35, 3385–3394, https://doi.org/10.1016/S1352-2310(01)00138-8, 2001.

Largeron, Y. and Staquet, C.: Persistent inversion dynamics and wintertime PM_{10} air pollution in Alpine valleys, Atmospheric Environment, 135, 92–108, https://doi.org/10.1016/j.atmosenv.2016.03.045, 2016.

Leighton, P. A.: Photochemistry of Air Pollution., 66, 1961.

Li, J., Zhang, X., Orlando, J., Tyndall, G., and Michalski, G.: Quantifying the nitrogen isotope effects during photochemical equilibrium between NO and NO_2: implications for $\delta^{15}N$ in tropospheric reactive nitrogen, Atmospheric Chemistry and Physics, 20, 9805–9819, https://doi.org/10.5194/acp-20-9805-2020, 2020.

Li, J., Davy, P., Harvey, M., Katzman, T., Mitchell, T., and Michalski, G.: Nitrogen isotopes in nitrate aerosols collected in the remote marine boundary layer: Implications for nitrogen isotopic fractionations among atmospheric reactive nitrogen species, Atmospheric Environment, 245, 118028, https://doi.org/10.1016/j.atmosenv.2020.118028, 2021a.

Li, K., Jacob, D. J., Liao, H., Qiu, Y., Shen, L., Zhai, S., Bates, K. H., Sulprizio, M. P., Song, S., Lu, X., Zhang, Q., Zheng, B., Zhang, Y., Zhang, J., Lee, H. C., and Kuk, S. K.: Ozone pollution in the North China Plain spreading into the late-winter haze season, Proceedings of the National Academy of Sciences, 118, e2015797118, https://doi.org/10.1073/pnas.2015797118, 2021b.

Li, Y., Shi, G., Chen, Z., Lan, M., Ding, M., Li, Z., and Hastings, M. G.: Significant Latitudinal Gradient of Nitrate Production in the Marine Atmospheric Boundary Layer of the Northern Hemisphere, Geophysical Research Letters, 49, e2022GL100503, https://doi.org/10.1029/2022GL100503, 2022a.

Li, Z., Walters, W. W., Hastings, M. G., Song, L., Huang, S., Zhu, F., Liu, D., Shi, G., Li, Y., and Fang, Y.: Atmospheric nitrate formation pathways in urban and rural atmosphere of Northeast China: Implications for complicated anthropogenic effects, Environmental Pollution, 296, 118752, https://doi.org/10.1016/j.envpol.2021.118752, 2022b.

Lim, S., Lee, M., Savarino, J., and Laj, P.: Oxidation pathways and emission sources of atmospheric particulate nitrate in Seoul: based on $\delta^{15}N$ and $\Delta^{17}O$ measurements, Atmospheric Chemistry and Physics, 22, 5099–5115, https://doi.org/10.5194/acp-22-5099-2022, 2022.

Liu, J., Liu, Z., Ma, Z., Yang, S., Yao, D., Zhao, S., Hu, B., Tang, G., Sun, J., Cheng, M., Xu, Z., and Wang, Y.: Detailed budget analysis of HONO in Beijing, China: Implication on atmosphere oxidation capacity in polluted megacity, Atmospheric Environment, 244, 117957, https://doi.org/10.1016/j.atmosenv.2020.117957, 2021.

Liu, Z., Hu, K., Zhang, K., Zhu, S., Wang, M., and Li, L.: VOCs sources and roles in O3 formation in the central Yangtze River Delta region of China, Atmospheric Environment, 302, 119755, https://doi.org/10.1016/j.atmosenv.2023.119755, 2023.

Luo, L., Wu, S., Zhang, R., Wu, Y., Li, J., and Kao, S.: What controls aerosol δ15N-NO3−? NOx emission sources vs. nitrogen isotope fractionation, Science of The Total Environment, 871, 162185, https://doi.org/10.1016/j.scitotenv.2023.162185, 2023.

Masson-Delmotte, V., Zhai, A., Pirani, A., Connors, S. L., Péan, C., Berger, S., Caud, N., Chen, Y., Goldfarb, L., Gomis, M. I., Huang, M., Leitzell, K., Lonnoy, E., Matthews, J. B. R., Maycock, T. K., Waterfield, T., Yelekçi, O., Yu, R., and Zhou, B.: In Climate Change 2021: The Physical Science Basis. Contribution of Working Group I to the Sixth Assessment Report of the Intergovernmental Panel on Climate Change, Cambridge University Press, Cambridge, United Kingdom and New York, NY, USA, 147–286, https://doi.org/10.1017/9781009157896.003, 2021.

Mayer, H.: Air pollution in cities, Atmospheric Environment, 33, 4029–4037, https://doi.org/10.1016/S1352-2310(99)00144-2, 1999.

McIlvin, M. R. and Altabet, M. A.: Chemical Conversion of Nitrate and Nitrite to Nitrous Oxide for Nitrogen and Oxygen Isotopic Analysis in Freshwater and Seawater, Analytical Chemistry, 77, 5589–5595, https://doi.org/10.1021/ac050528s, 2005.

Michalski, G., Scott, Z., Kabiling, M., and Thiemens, M. H.: First measurements and modeling of $\Delta^{17}O$ in atmospheric nitrate., Geophysical Research Letters, 30, 1870, https://doi.org/10.1029/2003GL017015, 2003.

Michalski, G., Bhattacharya, S. K., and Girsch, G.: NO_x cycle and the tropospheric ozone isotope anomaly: an experimental investigation, Atmospheric Chemistry and Physics, 14, 4935–4953, https://doi.org/10.5194/acp-14-4935-2014, 2014.

Michoud, V., Doussin, J.-F., Colomb, A., Afif, C., Borbon, A., Camredon, M., Aumont, B., Legrand, M., and Beekmann, M.: Strong HONO formation in a suburban site during snowy days, Atmospheric Environment, 116, 155–158, https://doi.org/10.1016/j.atmosenv.2015.06.040, 2015.

Miller, C. E. and Yung, Y. L.: Photo-induced isotopic fractionation, Journal of Geophysical Research: Atmospheres, 105, 29039–29051, https://doi.org/10.1029/2000JD900388, 2000.

Miller, D. J., Wojtal, P. K., Clark, S. C., and Hastings, M. G.: Vehicle NO_x emission plume isotopic signatures: Spatial variability across the eastern United States, Journal of Geophysical Research: Atmospheres, 122, 4698–4717, https://doi.org/10.1002/2016JD025877, 2017.

Miller, D. J., Chai, J., Guo, F., Dell, C. J., Karsten, H., and Hastings, M. G.: Isotopic Composition of In Situ Soil NO_x Emissions in Manure-Fertilized Cropland, Geophysical Research Letters, 45, 12,058-12,066, https://doi.org/10.1029/2018GL079619, 2018.

Morin, S., Savarino, J., Bekki, S., Cavender, A., Shepson, P. B., and Bottenheim, J. W.: Major influence of BrO on the NO_3 and nitrate budgets in the Arctic spring, inferred from $\Delta^{17}O(NO_3^-)$ measurements during ozone depletion events, Environ. Chem., 4, 238, https://doi.org/10.1071/EN07003, 2007a.

Morin, S., Savarino, J., Bekki, S., Gong, S., and Bottenheim, J. W.: Signature of Arctic surface ozone depletion events in the isotope anomaly ($\Delta^{17}O$) of atmospheric nitrate, Atmos. Chem. Phys., 7, 1451–1469, https://doi.org/10.5194/acp-7-1451-2007, 2007b.

Morin, S., Savarino, J., Frey, M. M., Domine, F., Jacobi, H.-W., Kaleschke, L., and Martins, J. M. F.: Comprehensive isotopic composition of atmospheric nitrate in the Atlantic Ocean boundary layer from 65°S to 79°N, Journal of Geophysical Research: Atmospheres, 114, https://doi.org/10.1029/2008JD010696, 2009.

Morin, S., Sander, R., and Savarino, J.: Simulation of the diurnal variations of the oxygen isotope anomaly ($\Delta^{17}O$) of reactive atmospheric species, Atmospheric Chemistry and Physics, 11, 3653–3671, https://doi.org/10.5194/acp-11-3653-2011, 2011.

Newsome, B. and Evans, M.: Impact of uncertainties in inorganic chemical rate constants on tropospheric composition and ozone radiative forcing, Atmos. Chem. Phys., 17, 14333–14352, https://doi.org/10.5194/acp-17-14333-2017, 2017.

Olofson, K. F. G., Andersson, P. U., Hallquist, M., Ljungström, E., Tang, L., Chen, D., and Pettersson, J. B. C.: Urban aerosol evolution and particle formation during wintertime temperature inversions, Atmospheric Environment, 43, 340–346, https://doi.org/10.1016/j.atmosenv.2008.09.080, 2009.

ORCAE: Rapport des profils climat air énergie de la communauté de communes de la Vallée de Chamonix-Mont-Blanc, https://www.orcae-auvergne-rhone-alpes.fr/, 2022.

Park, R. J., Jacob, D. J., Field, B. D., Yantosca, R. M., and Chin, M.: Natural and transboundary pollution influences on sulfate-nitrate-ammonium aerosols in the United States: Implications for policy, Journal of Geophysical Research: Atmospheres, 109, https://doi.org/10.1029/2003JD004473, 2004.

Patris, N., Cliff, S., Quinn, P., Kasem, M., and Thiemens, M.: Isotopic analysis of aerosol sulfate and nitrate during ITCT-2k2: Determination of different formation pathways as a function of particle size, Journal of Geophysical Research, 112, https://doi.org/10.1029/2005JD006214, 2007.

Penkett, S. A., Burgess, R. A., Coe, H., Coll, I., Hov, Ø., Lindskog, A., Schmidbauer, N., Solberg, S., Roemer, M., Thijsse, T., Beck, J., and Reeves, C. E.: Evidence for large average concentrations of the nitrate radical (NO_3) in Western Europe from the HANSA hydrocarbon database, Atmospheric Environment, 41, 3465–3478, https://doi.org/10.1016/j.atmosenv.2006.11.055, 2007.

Prabhakar, G., Parworth, C. L., Zhang, X., Kim, H., Young, D. E., Beyersdorf, A. J., Ziemba, L. D., Nowak, J. B., Bertram, T. H., Faloona, I. C., Zhang, Q., and Cappa, C. D.: Observational assessment of the role of nocturnal residual-layer chemistry in determining daytime surface particulate nitrate concentrations, Atmospheric Chemistry and Physics, 17, 14747–14770, https://doi.org/10.5194/acp-17-14747-2017, 2017.

Prospero, J. M. and Savoie, D. L.: Effect of continental sources on nitrate concentrations over the Pacific Ocean, Nature, 339, 687–689, https://doi.org/10.1038/339687a0, 1989.

Pugh, T. A. M., Cain, M., Methven, J., Wild, O., Arnold, S. R., Real, E., Law, K. S., Emmerson, K. M., Owen, S. M., Pyle, J. A., Hewitt, C. N., and MacKenzie, A. R.: A Lagrangian model of air-mass photochemistry and mixing using a trajectory ensemble: the Cambridge Tropospheric Trajectory model of Chemistry And Transport (CiTTyCAT) version 4.2, Geosci. Model Dev., 5, 193–221, https://doi.org/10.5194/gmd-5-193-2012, 2012.

Quimbayo-Duarte, J., Chemel, C., Staquet, C., Troude, F., and Arduini, G.: Drivers of severe air pollution events in a deep valley during wintertime: A case study from the Arve river valley, France, Atmospheric Environment, 247, 118030, https://doi.org/10.1016/j.atmosenv.2020.118030, 2021.

Ren, J., Guo, F., and Xie, S.: Diagnosing ozone–NO $_x$ –VOC sensitivity and revealing causes of ozone increases in China based on 2013–2021 satellite retrievals, Atmos. Chem. Phys., 22, 15035–15047, https://doi.org/10.5194/acp-22-15035-2022, 2022.

Ren, X., Brune, W. H., Mao, J., Mitchell, M. J., Lesher, R. L., Simpas, J. B., Metcalf, A. R., Schwab, J. J., Cai, C., Li, Y., Demerjian, K. L., Felton, H. D., Boynton, G., Adams, A., Perry, J., He, Y., Zhou, X., and Hou, J.: Behavior of OH and HO_2 in the winter atmosphere in New York City, Atmospheric Environment, 40, 252–263, https://doi.org/10.1016/j.atmosenv.2005.11.073, 2006.

Richard, L., Romanini, D., and Ventrillard, I.: Nitric Oxide Analysis Down to ppt Levels by Optical-Feedback Cavity-Enhanced Absorption Spectroscopy, Sensors, 18, 1997, https://doi.org/10.3390/s18071997, 2018.

Savard, M. M., Cole, A. S., Vet, R., and Smirnoff, A.: The $\Delta^{17}O$ and $\delta^{18}O$ values of atmospheric nitrates simultaneously collected downwind of anthropogenic sources – implications for polluted air masses, Atmospheric Chemistry and Physics, 18, 10373–10389, https://doi.org/10.5194/acp-18-10373-2018, 2018.

Savarino, J., Kaiser, J., Morin, S., Sigman, D. M., and Thiemens, M. H.: Nitrogen and oxygen isotopic constraints on the origin of atmospheric nitrate in coastal Antarctica, Atmos. Chem. Phys., 21, 2007.

Savarino, J., Bhattacharya, S. K., Morin, S., Baroni, M., and Doussin, J.-F.: The $NO+O_3$ reaction: A triple oxygen isotope perspective on the reaction dynamics and atmospheric implications for the transfer of the ozone isotope anomaly, J. Chem. Phys., 128, 194303, https://doi.org/10.1063/1.2917581, 2008.

Savarino, J., Morin, S., Erbland, J., Grannec, F., Patey, M. D., Vicars, W., Alexander, B., and Achterberg, E. P.: Isotopic composition of atmospheric nitrate in a tropical marine boundary layer, PNAS, 110, 17668–17673, https://doi.org/10.1073/pnas.1216639110, 2013.

Savarino, J., Vicars, W. C., Legrand, M., Preunkert, S., Jourdain, B., Frey, M. M., Kukui, A., Caillon, N., and Roca, J. G.: Oxygen isotope mass balance of atmospheric nitrate at Dome C, East Antarctica, during the OPALE campaign, Atmos. Chem. Phys., 16, 2016.

Schaap, M., Müller, K., and ten Brink, H. M.: Constructing the European aerosol nitrate concentration field from quality analysed data, Atmospheric Environment, 36, 1323–1335, https://doi.org/10.1016/S1352-2310(01)00556-8, 2002.

Schwikowski, M., Seibert, P., Baltensperger, U., and Gaggeler, H. W.: A study of an outstanding Saharan dust event at the high-alpine site Jungfraujoch, Switzerland, Atmospheric Environment, 29, 1829–1842, https://doi.org/10.1016/1352-2310(95)00060-C, 1995.

Shah, V., Jaeglé, L., Thornton, J. A., Lopez-Hilfiker, F. D., Lee, B. H., Schroder, J. C., Campuzano-Jost, P., Jimenez, J. L., Guo, H., Sullivan, A. P., Weber, R. J., Green, J. R., Fiddler, M. N., Bililign, S., Campos, T. L., Stell, M., Weinheimer, A. J., Montzka, D. D., and Brown, S. S.: Chemical feedbacks weaken the wintertime response of particulate sulfate and nitrate to

emissions reductions over the eastern United States, Proc Natl Acad Sci USA, 115, 8110–8115, https://doi.org/10.1073/pnas.1803295115, 2018.

Sharma, H. D., Jervis, R. E., and Wong, K. Y.: Isotopic exchange reactions in nitrogen oxides, J. Phys. Chem., 74, 923–933, https://doi.org/10.1021/j100699a044, 1970.

Shi, X., Nenes, A., Xiao, Z., Song, S., Yu, H., Shi, G., Zhao, Q., Chen, K., Feng, Y., and Russell, A. G.: High-Resolution Data Sets Unravel the Effects of Sources and Meteorological Conditions on Nitrate and Its Gas-Particle Partitioning, Environ. Sci. Technol., 53, 3048–3057, https://doi.org/10.1021/acs.est.8b06524, 2019.

Sigman, D. M., Casciotti, K. L., Andreani, M., Barford, C., Galanter, M., and Böhlke, J. K.: A Bacterial Method for the Nitrogen Isotopic Analysis of Nitrate in Seawater and Freshwater, Analytical Chemistry, 73, 4145–4153, https://doi.org/10.1021/ac010088e, 2001.

Simpson, W. R., Brown, S. S., Saiz-Lopez, A., Thornton, J. A., and von Glasow, R.: Tropospheric Halogen Chemistry: Sources, Cycling, and Impacts, Chem. Rev., 115, 4035–4062, https://doi.org/10.1021/cr5006638, 2015.

Sodemann, H., Palmer, A. S., Schwierz, C., Schwikowski, M., and Wernli, H.: The transport history of two Saharan dust events archived in an Alpine ice core, Atmospheric Chemistry and Physics, 6, 667–688, https://doi.org/10.5194/acp-6-667-2006, 2006.

Song, W., Liu, X.-Y., Houlton, B. Z., and Liu, C.-Q.: Isotopic constraints confirm the significant role of microbial nitrogen oxides emissions from the land and ocean environment, National Science Review, 9, nwac106, https://doi.org/10.1093/nsr/nwac106, 2022.

Stone, D., Whalley, L. K., and Heard, D. E.: Tropospheric OH and HO2 radicals: field measurements and model comparisons, Chem. Soc. Rev., 41, 6348–6404, https://doi.org/10.1039/C2CS35140D, 2012.

Tan, Z., Rohrer, F., Lu, K., Ma, X., Bohn, B., Broch, S., Dong, H., Fuchs, H., Gkatzelis, G. I., Hofzumahaus, A., Holland, F., Li, X., Liu, Y., Liu, Y., Novelli, A., Shao, M., Wang, H., Wu, Y., Zeng, L., Hu, M., Kiendler-Scharr, A., Wahner, A., and Zhang, Y.: Wintertime photochemistry in Beijing: observations of RO_x radical concentrations in the North China Plain during the BEST-ONE campaign, Atmos. Chem. Phys., 18, 12391–12411, https://doi.org/10.5194/acp-18-12391-2018, 2018.

Thiemens, M. H.: History and Applications of Mass-independent Isotope Effects, Annual Review of Earth and Planetary Sciences, 34, 217–262, https://doi.org/10.1146/annurev.earth.34.031405.125026, 2006.

Thornton, J. A., Kercher, J. P., Riedel, T. P., Wagner, N. L., Cozic, J., Holloway, J. S., Dubé, W. P., Wolfe, G. M., Quinn, P. K., Middlebrook, A. M., Alexander, B., and Brown, S. S.: A large atomic chlorine source inferred from mid-continental reactive nitrogen chemistry, Nature, 464, 271–274, https://doi.org/10.1038/nature08905, 2010.

Tørseth, K., Aas, W., Breivik, K., Fjæraa, A. M., Fiebig, M., Hjellbrekke, A. G., Lund Myhre, C., Solberg, S., and Yttri, K. E.: Introduction to the European Monitoring and Evaluation Programme (EMEP) and observed atmospheric composition change during 1972-2009, Atmospheric Chemistry and Physics, 12, 5447–5481, https://doi.org/10.5194/acp-12-5447-2012, 2012.

Tsimpidi, A. P., Karydis, V. A., and Pandis, S. N.: Response of Fine Particulate Matter to Emission Changes of Oxides of Nitrogen and Anthropogenic Volatile Organic Compounds in the Eastern United States, Journal of the Air & Waste Management Association, 58, 1463–1473, https://doi.org/10.3155/1047-3289.58.11.1463, 2008.

Usher, C. R., Michel, A. E., and Grassian, V. H.: Reactions on Mineral Dust, Chem. Rev., 103, 4883–4940, https://doi.org/10.1021/cr020657y, 2003.

Vicars, W. C. and Savarino, J.: Quantitative constraints on the ^{17}O-excess (Δ^{17}O) signature of surface ozone: Ambient measurements from 50°N to 50°S using the nitrite-coated filter technique, Geochimica et Cosmochimica Acta, 135, 270–287, https://doi.org/10.1016/j.gca.2014.03.023, 2014.

Vicars, W. C., Bhattacharya, S. K., Erbland, J., and Savarino, J.: Measurement of the 17O-excess (Δ17O) of tropospheric ozone using a nitrite-coated filter, Rapid Communications in Mass Spectrometry, 26, 1219–1231, https://doi.org/10.1002/rcm.6218, 2012.

Vicars, W. C., Morin, S., Savarino, J., Wagner, N. L., Erbland, J., Vince, E., Martins, J. M. F., Lerner, B. M., Quinn, P. K., Coffman, D. J., Williams, E. J., and Brown, S. S.: Spatial and diurnal variability in reactive nitrogen oxide chemistry as reflected in the isotopic composition of atmospheric nitrate: Results from the CalNex 2010 field study, Journal of Geophysical Research: Atmospheres, 118, 10,567-10,588, https://doi.org/10.1002/jgrd.50680, 2013.

Vitousek, P. M., Aber, J. D., Howarth, R. W., Likens, G. E., Matson, P. A., Schindler, D. W., Schlesinger, W. H., and Tilman, D. G.: Human Alteration of the Global Nitrogen Cycle: Sources and Consequences, Ecological Applications, 7, 737–750, https://doi.org/10.1890/1051-0761(1997)007[0737:HAOTGN]2.0.CO;2, 1997.

Walters, W. W. and Michalski, G.: Theoretical calculation of nitrogen isotope equilibrium exchange fractionation factors for various NO_y molecules, Geochimica et Cosmochimica Acta, 164, 284–297, https://doi.org/10.1016/j.gca.2015.05.029, 2015.

Walters, W. W. and Michalski, G.: Theoretical calculation of oxygen equilibrium isotope fractionation factors involving various NO_y molecules, OH, and H_2O and its implications for isotope variations in atmospheric nitrate, Geochimica et Cosmochimica Acta, 191, 89–101, https://doi.org/10.1016/j.gca.2016.06.039, 2016.

Walters, W. W., Tharp, B. D., Fang, H., Kozak, B. J., and Michalski, G.: Nitrogen isotope composition of thermally produced NO_x from various fossil-fuel combustion sources, Environmental Science & Technology, 49, 11363–11371, https://doi.org/10.1021/acs.est.5b02769, 2015a.

Walters, W. W., Goodwin, S. R., and Michalski, G.: Nitrogen Stable Isotope Composition (δ^{15}N) of Vehicle-Emitted NO_x, Environ. Sci. Technol., 49, 2278–2285, https://doi.org/10.1021/es505580v, 2015b.

Walters, W. W., Simonini, D. S., and Michalski, G.: Nitrogen isotope exchange between NO and NO_2 and its implications for δ^{15}N variations in tropospheric NO_x and atmospheric nitrate, Geophysical Research Letters, 43, 440–448, https://doi.org/10.1002/2015GL066438, 2016.

Walters, W. W., Fang, H., and Michalski, G.: Summertime diurnal variations in the isotopic composition of atmospheric nitrogen dioxide at a small midwestern United States city, Atmospheric Environment, 179, 1–11, https://doi.org/10.1016/j.atmosenv.2018.01.047, 2018.

Wang, X., Jacob, D. J., Eastham, S. D., Sulprizio, M. P., Zhu, L., Chen, Q., Alexander, B., Sherwen, T., Evans, M. J., Lee, B. H., Haskins, J. D., Lopez-Hilfiker, F. D., Thornton, J. A., Huey, G. L., and Liao, H.: The role of chlorine in global tropospheric chemistry, Atmospheric Chemistry and Physics, 19, 3981–4003, https://doi.org/10.5194/acp-19-3981-2019, 2019a.

Wang, Y., Zhang, Q. Q., He, K., Zhang, Q., and Chai, L.: Sulfate-nitrate-ammonium aerosols over China: response to 2000–2015 emission changes of sulfur dioxide, nitrogen oxides, and ammonia, Atmospheric Chemistry and Physics, 13, 2635–2652, https://doi.org/10.5194/acp-13-2635-2013, 2013.

Wang, Y., Gao, W., Wang, S., Song, T., Gong, Z., Ji, D., Wang, L., Liu, Z., Tang, G., Huo, Y., Tian, S., Li, J., Li, M., Yang, Y., Chu, B., Petäjä, T., Kerminen, V.-M., He, H., Hao, J., Kulmala, M., Wang, Y., and Zhang, Y.: Contrasting trends of $PM_{2.5}$ and surface-ozone concentrations in China from 2013 to 2017, National Science Review, 7, 1331–1339, https://doi.org/10.1093/nsr/nwaa032, 2020.

Wang, Y., Liu, J., Jiang, F., Chen, Z., Wu, L., Zhou, S., Pei, C., Kuang, Y., Cao, F., Zhang, Y., Fan, M., Zheng, J., Li, J., and Zhang, G.: Vertical measurements of stable nitrogen and oxygen isotope composition of fine particulate nitrate aerosol in Guangzhou city: Source apportionment and oxidation pathway, Science of The Total Environment, 865, 161239, https://doi.org/10.1016/j.scitotenv.2022.161239, 2023.

Wang, Y. L., Song, W., Yang, W., Sun, X. C., Tong, Y. D., Wang, X. M., Liu, C. Q., Bai, Z. P., and Liu, Z. Y.: Influences of Atmospheric Pollution on the Contributions of Major Oxidation Pathways to $PM_{2.5}$ Nitrate Formation in Beijing, Journal of Geophysical Research: Atmospheres, 124, 4174–4185, https://doi.org/10.1029/2019JD030284, 2019b.

Wayne, R. P., Barnes, I., Biggs, P., Burrows, J. P., Canosa-Mas, C. E., Hjorth, J., Le Bras, G., Moortgat, G. K., Perner, D., Poulet, G., Restelli, G., and Sidebottom, H.: The nitrate radical: Physics, chemistry, and the atmosphere, Atmospheric Environment. Part A. General Topics, 25, 1–203, https://doi.org/10.1016/0960-1686(91)90192-A, 1991.

Weber, S., Uzu, G., Calas, A., Chevrier, F., Besombes, J.-L., Charron, A., Salameh, D., Ježek, I., Močnik, G., and Jaffrezo, J.-L.: An apportionment method for the oxidative potential of atmospheric particulate matter sources: application to a one-year study in Chamonix, France, Atmospheric Chemistry and Physics, 18, 9617–9629, https://doi.org/10.5194/acp-18-9617-2018, 2018.

Whiteman, C. D.: Breakup of Temperature Inversions in Deep Mountain Valleys: Part I. Observations, Journal of Applied Meteorology and Climatology, 21, 270–289, https://doi.org/10.1175/1520-0450(1982)021<0270:BOTIID>2.0.CO;2, 1982.

WHO: Whorld Health Organization global air quality guidelines: particulate matter ($PM_{2.5}$ and PM_{10}), ozone, nitrogen dioxide, sulfur dioxide and carbon monoxide, 2021.

Wild, O., Zhu, X., and Prather, M. J.: Fast-J: Accurate simulation of in- and below-cloud photolysis in tropospheric chemical models, Journal of Atmospheric Chemistry, 37, 245–282, https://doi.org/10.1023/A:1006415919030, 2000.

Xue, C.: Substantially Growing Interest in the Chemistry of Nitrous Acid (HONO) in China: Current Achievements, Problems, and Future Directions, Environ. Sci. Technol., 56, 7375–7377, https://doi.org/10.1021/acs.est.2c02237, 2022.

Young, E. D., Galy, A., and Nagahara, H.: Kinetic and equilibrium mass-dependent isotope fractionation laws in nature and their geochemical and cosmochemical significance, Geochimica et Cosmochimica Acta, 66, 1095–1104, https://doi.org/10.1016/S0016-7037(01)00832-8, 2002.

Yu, Z. and Elliott, E. M.: Novel Method for Nitrogen Isotopic Analysis of Soil-Emitted Nitric Oxide, Environ. Sci. Technol., 51, 6268–6278, https://doi.org/10.1021/acs.est.7b00592, 2017.

Zhang, L., Vet, R., O'Brien, J. M., Mihele, C., Liang, Z., and Wiebe, A.: Dry deposition of individual nitrogen species at eight Canadian rural sites, Journal of Geophysical Research: Atmospheres, 114, https://doi.org/10.1029/2008JD010640, 2009.

Zhang, R., Wang, G., Guo, S., Zamora, M. L., Ying, Q., Lin, Y., Wang, W., Hu, M., and Wang, Y.: Formation of Urban Fine Particulate Matter, Chem. Rev., 115, 3803–3855, https://doi.org/10.1021/acs.chemrev.5b00067, 2015.

Zhang, W., Bi, X., Zhang, Y., Wu, J., and Feng, Y.: Diesel vehicle emission accounts for the dominate NO_x source to atmospheric particulate nitrate in a coastal city: Insights from nitrate dual isotopes of $PM_{2.5}$, Atmospheric Research, 278, 106328, https://doi.org/10.1016/j.atmosres.2022.106328, 2022a.

Zhang, Y.-L., Zhang, W., Fan, M.-Y., Li, J., Fang, H., Cao, F., Lin, Y.-C., Wilkins, B. P., Liu, X., Bao, M., Hong, Y., and Michalski, G.: A diurnal story of $\Delta^{17}O(NO_3^-)$ in urban Nanjing and its implication for nitrate aerosol formation, npj Clim Atmos Sci, 5, 1–10, https://doi.org/10.1038/s41612-022-00273-3, 2022b.

Zhou, W., Gao, M., He, Y., Wang, Q., Xie, C., Xu, W., Zhao, J., Du, W., Qiu, Y., Lei, L., Fu, P., Wang, Z., Worsnop, D. R., Zhang, Q., and Sun, Y.: Response of aerosol chemistry to clean air action in Beijing, China: Insights from two-year ACSM measurements and model simulations, Environmental Pollution, 255, 113345, https://doi.org/10.1016/j.envpol.2019.113345, 2019.

Zong, Z., Wang, X., Tian, C., Chen, Y., Fang, Y., Zhang, F., Li, C., Sun, J., Li, J., and Zhang, G.: First Assessment of NOx Sources at a Regional Background Site in North China Using Isotopic Analysis Linked with Modeling, Environmental Science and Technology, 51, 5923–5931, https://doi.org/10.1021/acs.est.6b06316, 2017.

Zong, Z., Sun, Z., Xiao, L., Tian, C., Liu, J., Sha, Q., Li, J., Fang, Y., Zheng, J., and Zhang, G.: Insight into the Variability of the Nitrogen Isotope Composition of Vehicular NO_x in China, Environ. Sci. Technol., acs.est.0c04749, https://doi.org/10.1021/acs.est.0c04749, 2020.